Monthly Notices of the ROYAL ASTRONOMICAL SOCIETY

MNRAS **512,** 4210–4230 (2022) https://doi.org/10.1093/mnras/stac672
Advance Access publication 2022 March 11

A MeerKAT-meets-LOFAR study of MS 1455.0 + 2232: a 590 kiloparsec 'mini'-halo in a sloshing cool-core cluster

C. J. Riseley [1,2,3]★ K. Rajpurohit [1,2,4] F. Loi [5] A. Botteon [6] R. Timmerman,[6] N. Biava [1,2] A. Bonafede,[1,2] E. Bonnassieux,[1,2] G. Brunetti,[2] T. Enßlin,[7] G. Di Gennaro,[8] A. Ignesti,[9] T. Shimwell,[6] C. Stuardi,[1,2] T. Vernstrom [3,10] and R. J. van Weeren[6]

[1]*Dipartimento di Fisica e Astronomia, Università degli Studi di Bologna, via P. Gobetti 93/2, I-40129 Bologna, Italy*
[2]*INAF – Istituto di Radioastronomia, via P. Gobetti 101, I-40129 Bologna, Italy*
[3]*CSIRO Space & Astronomy, PO Box 1130, Bentley, WA 6102, Australia*
[4]*Thüringer Landessternwarte, Sternwarte 5, D-07778 Tautenburg, Germany*
[5]*INAF-Osservatorio Astronomico di Cagliari, Via della Scienza 5, I-09047 Selargius, CA, Italy*
[6]*Leiden Observatory, Leiden University, P.O. Box 9513, NL-2300 RA Leiden, the Netherlands*
[7]*Max Planck Institute for Astrophysics, Karl-Schwarzschild-Straße 1, D-85748 Garching, Germany*
[8]*Hamburger Sternwarte, Universität Hamburg, Gojenbergsweg 112, D-21029 Hamburg, Germany*
[9]*INAF – Astronomical Observatory of Padova, vicolo dell'Osservatorio 5, I-35122 Padova, Italy*
[10]*ICRAR, The University of Western Australia, 35 Stirling Hw, 6009 Crawley, Australia*

Accepted 2022 March 9. Received 2022 March 7; in original form 2021 December 13

ABSTRACT

Radio mini-haloes are poorly understood, moderately extended diffuse radio sources that trace the presence of magnetic fields and relativistic electrons on scales of hundreds of kiloparsecs, predominantly in relaxed clusters. With relatively few confirmed detections to-date, many questions remain unanswered. This paper presents new radio observations of the galaxy cluster MS 1455.0+2232 performed with MeerKAT (covering the frequency range 872−1712 MHz) and LOFAR (covering 120−168 MHz), the first results from a homogeneously selected mini-halo census. We find that this mini-halo extends for ∼590 kpc at 1283 MHz, significantly larger than previously believed, and has a flatter spectral index ($\alpha = -0.97 \pm 0.05$) than typically expected. Our X-ray analysis clearly reveals a large-scale (254 kpc) sloshing spiral in the intracluster medium. We perform a point-to-point analysis, finding a tight single correlation between radio and X-ray surface brightness with a super-linear slope of $b_{1283\,\mathrm{MHz}} = 1.16^{+0.06}_{-0.07}$ and $b_{145\,\mathrm{MHz}} = 1.15^{+0.09}_{-0.08}$; this indicates a strong link between the thermal and non-thermal components of the intracluster medium. Conversely, in the spectral index/X-ray surface brightness plane, we find that regions inside and outside the sloshing spiral follow different correlations. We find compelling evidence for multiple sub-components in this mini-halo for the first time. While both the turbulent (re-)acceleration and hadronic scenarios are able to explain some observed properties of the mini-halo in MS 1455.0+2232, neither scenario is able to account for all the evidence presented by our analysis.

Key words: galaxies: clusters: general – galaxies: clusters: individual: MS 1455.0+2232 – galaxies: clusters: intracluster medium – radio continuum: general – X-rays: galaxies: clusters.

1 INTRODUCTION

The intracluster medium (ICM) constitutes some 80 per cent of the baryonic mass of a galaxy cluster, comprising a hot ($T \sim 10^7$–10^8 K) tenuous ($n_e \sim 10^{-3}$ cm^{-3}) plasma, which emits at X-ray wavelengths via Bremsstrahlung emission. During cluster merger events, tremendous quantities of energy (∼10^{64} erg; Ferrari et al. 2008) are deposited into the ICM via shocks and turbulence. Many merging clusters are known to host embedded radio galaxies which, when resolved, show clear evidence of interaction with the ICM (e.g. Mao et al. 2009; Douglass et al. 2011; Pratley et al. 2013; Owen et al. 2014; van Weeren et al. 2017; Wilber et al. 2018; Clarke et al. 2019; Botteon et al. 2020b, 2021; Bonafede et al. 2021; de Gasperin et al. 2022). On larger scales, many merging clusters host spectacular sources of diffuse radio emission, broadly classified as 'radio haloes' and 'radio relics' (see van Weeren et al. 2019, for a recent review). There is a third class of diffuse radio source – 'radio mini-haloes', a term first introduced by Feretti & Giovannini (1996) – which have to-date been detected primarily in relaxed clusters, suggesting that major mergers are not the key ingredient in generating a mini-halo. Given the typically short synchrotron lifetime of relativistic electrons ($\tau \lesssim 10^8$ yr) compared to the spatial scales over which the diffuse radio emission is detected, all three broad classes of non-thermal phenomena associated with the ICM require *in situ* acceleration (Jaffe 1977).

Mini-haloes remain the most poorly understood class as they are relatively rare objects, with only some 32 currently known, compared to around ∼72 clusters hosting radio relics and ∼95 hosting radio

★ E-mail: christopher.riseley@unibo.it

© 2022 The Author(s)
Published by Oxford University Press on behalf of Royal Astronomical Society

Downloaded from https://academic.oup.com/mnras/article/512/3/4210/6547010 by guest on 07 March 2025

haloes (van Weeren et al. 2019). We note however that with the advent of many next-generation radio interferometers, the known population of diffuse radio sources in clusters of galaxies is expanding dramatically (for example, Govoni et al. 2019; Botteon et al. 2020a; Duchesne, Johnston-Hollitt & Bartalucci 2021b; Hodgson et al. 2021; Osinga et al. 2021; van Weeren et al. 2021; Duchesne et al. 2022; Knowles et al. 2022). Mini-haloes are moderately extended (typically $\sim$0.1$-$0.3 Mpc), steep-spectrum ($\alpha \lesssim -1$, where α is the spectral index, relating flux density S to observing frequency ν as $S \propto \nu^{\alpha}$) objects that are centrally located in relaxed clusters which also host a radio source associated with the nucleus of the brightest cluster galaxy (BCG).

Much discussion has occurred over the past two decades in the literature regarding the nature of the acceleration mechanism responsible for powering the relativistic electrons that generate mini-haloes. Two principal mechanisms exist: turbulent (re-)acceleration (Gitti, Brunetti & Setti 2002; ZuHone et al. 2013) and hadronic processes (Pfrommer & Enßlin 2004).

The turbulent (re-)acceleration scenario implies a careful balance between injecting sufficient turbulence to induce large-scale gas sloshing motions, while also leaving the relaxed cool core intact. Simulations generally suggest that minor and/or off-axis mergers can provide the necessary energy input (e.g. ZuHone et al. 2013), and observations have shown that mini-haloes tend to be bounded by cold fronts (see for example Mazzotta et al. 2001a,b; Mazzotta & Giacintucci 2008; Ghizzardi, Rossetti & Molendi 2010; Rossetti et al. 2013), suggesting sloshing motions that would introduce turbulence. Indeed, under reasonable conditions, theoretical predictions are able to match the observed variations in spectral index (Giacintucci et al. 2014). Finally, the co-location of many mini-haloes with the radio BCG may suggest a natural source for the seed population of mildly relativistic electrons that would be re-accelerated to the relativistic regime (e.g. Fujita et al. 2007). The correlations between mini-halo and BCG radio power, as well as mini-halo power and X-ray cavity power, provide further observational support for this scenario (Bravi, Gitti & Brunetti 2016; Richard-Laferrière et al. 2020).

In the hadronic scenario, cosmic ray electrons (CRe) are continuously injected via inelastic collisions between cosmic ray protons (CRp) and the cluster thermal proton population. CRp are expected to persist at some level throughout the cluster volume, being injected by active galactic nuclei (AGNs) and supernovae processes (for a comprehensive review, see Brunetti & Jones 2014). For giant radio haloes, purely hadronic models cannot work: one of the arguments against this scenario comes from *Fermi* upper limits to γ-ray emission from giant halo clusters, which are too constraining (e.g. Brunetti, Zimmer & Zandanel 2017). However, it has been recently shown by Ignesti et al. (2020) that the current limits from *Fermi* are compatible with the hadronic scenario in mini-halo clusters.

Hadronic models generally predict a smaller range of observed spectral index values ($-1.2 \lesssim \alpha \lesssim -1$; Pfrommer & Enßlin 2004; Brunetti & Jones 2014; ZuHone et al. 2015). Conversely, the turbulent (re-)acceleration scenario can yield a much broader range, including ultra-steep spectral indices ($\alpha \lesssim -1.5$; Brunetti et al. 2008; ZuHone et al. 2013; Brunetti & Jones 2014). Under the assumption of homogeneous conditions throughout the mini-halo, the turbulent (re-)acceleration scenario should lead to an observable spectral break towards high frequencies (due to the cutoff in the electron energy distribution). The presence of a high-frequency spectral break remains an open question, however. Few studies have the necessary high-quality high-frequency data, although some mini-haloes appear to show power-law spectra up to at least 10$-$20 GHz (Perrott et al. 2021; Timmerman et al. 2021).

Despite the differences in formation scenario, both scenarios do share some commonalities: the important role of cluster-member AGN (particularly the BCG) in providing seed particles, and the likely connection between the thermal and non-thermal components in the ICM. As such, correlations are expected between various probes of these components (e.g. radio and X-ray surface brightness). Recent work by Ignesti et al. (2020) attempted to investigate the statistical properties of the radio/X-ray connection for seven mini-haloes. Contrary to what is typically found in point-to-point correlation studies of giant haloes, Ignesti et al. (2020) found that mini-haloes tend to exhibit a super-linear correlation between radio surface brightness and X-ray surface brightness, i.e. $b > 1$ for $I_{\rm radio} \propto I^{b}_{\rm X-ray}$. However, their sample also showed significant scatter and relatively large uncertainty in the correlation slope b, largely due to the resolution of the available data (see also discussion by Bruno et al. 2021). Additionally, no statistically significant sample of high-quality mini-halo spectra exist, meaning no robust conclusions can be drawn regarding the spectral properties or the underlying acceleration mechanism.

Recently, the picture has become far more complex with new highly sensitive long-wavelength observations from the LOw-Frequency ARray (LOFAR; van Haarlem et al. 2013) revealing diffuse radio emission far outside the cool core of a handful of mini-halo clusters (Savini et al. 2018, 2019; Biava et al. 2021). These complex (ultra-)steep spectrum sources challenge the strict divide that has historically existed between mini-haloes and larger-scale haloes, and hint at different particle acceleration mechanisms being dominant on different scales. We also note that mini-haloes are not the only objects which show evidence of such complexity. Bonafede et al. (2014) detected a giant ($\sim$1.1 Mpc) radio halo in the cool-core cluster CL 1821+643. Additionally, the 'radio halo' in Abell 2142 exhibits evidence of substructure, including a brighter central component of mini-halo-like emission that blends into larger-scale diffuse halo-like emission (Venturi et al. 2017).

We are using deep observations with MeerKAT (Jonas & MeerKAT Team 2016)[1] covering the frequency range 872–1712 MHz, and the LOFAR High Band Antenna (HBA), covering the frequency range 120–168 MHz, to perform a multifrequency census of all known radio mini-haloes in the Declination range -1° to $+30^{\circ}$. The MeerKAT project code is MKT-20126 (P.I. Riseley). This multifrequency data are augmented by archival X-ray data from *Chandra* and *XMM-Newton*. The primary goal of our census is to determine the nature of particle acceleration mechanisms at play in mini-haloes using the first uniformly constructed mini-halo sample. This paper presents new results on the mini-halo in the cluster MS 1455.0+2232, carried out as a pilot study for our census.

In the next section, we will briefly summarize what is currently known about MS 1455.0+2232. The remainder of this paper is divided as follows: we discuss the observations and data reduction in Section 2, we present our results in Section 3 and analyse them in Section 4. In Section 5, we discuss our results in the context of the two principal acceleration scenarios. We draw our conclusions in Section 6. Throughout, we assume a ΛCDM cosmology of $H_0 = 73$ km s^{-1} Mpc^{-1}, $\Omega_{\rm m} = 0.27$, $\Omega_{\rm vac} = 0.73$. Given our cosmology, at the redshift of MS 1455.0+2232 ($z = 0.258$; Allen et al. 1992), an angular distance of 1 arcsec corresponds to a physical distance of 3.859 kpc. All uncertainties are quoted at the 1σ level.

[1]The technical capabilities of MeerKAT are also discussed further by Camilo et al. (2018) and Mauch et al. (2020).

Downloaded from https://academic.oup.com/mnras/article/512/3/4210/6547010 by guest on 07 March 2025

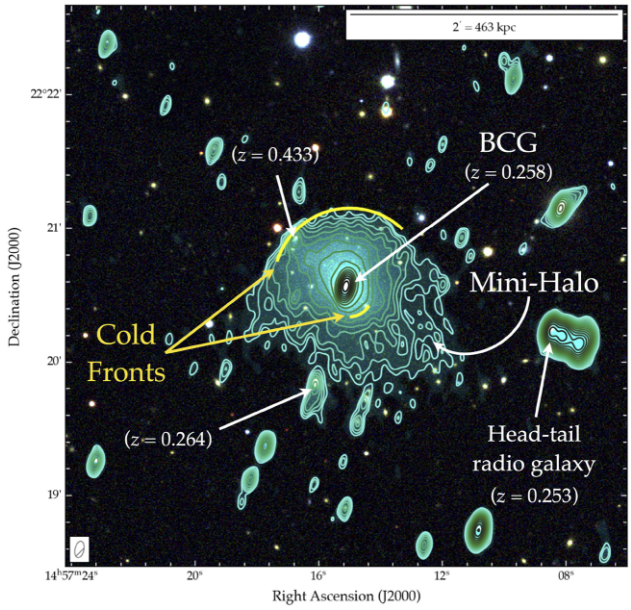


Figure 1. Colour-composite image of MS 1455.0+2232, showing 1283 MHz radio surface brightness measured by MeerKAT at 7.4 × 4.0 arcsec^2 resolution (teal colour and contours) overlaid on an optical RGB image constructed using *i*-, *r*-, and *g*-band images from SDSS DR16 (Ahumada et al. 2020). Contours start at 4σ and scale by a factor $\sqrt{2}$, where $\sigma = 5.9$ μJy beam^{-1}; see Table 1. The two known cold fronts identified by Mazzotta et al. (2001a) are shown with yellow arcs; the redshifts of selected galaxies are also shown.

1.1 The Mini-Halo in MS 1455.0+2232

MS 1455.0+2232 (also commonly referred to in the literature as Z7160 or ZwCl 1454.8+2233) is a cool-core cluster hosting a pair of cold fronts on opposing sides of the cluster centre (Mazzotta et al. 2001a; Mazzotta & Giacintucci 2008). The position of these cold fronts relative to the larger-scale emission from MS 1455.0+2232 is presented in Fig. 1. We show an illustrative colour-composite image, with our 1283 MHz MeerKAT map overlaid on an optical RGB image reconstructed using *i*-, *r*-, and *g*-band images from the Sloan Digital Sky Survey (SDSS) Data Release 16 (Ahumada et al. 2020).

This cluster has a mass of $M_{500} = (3.5 \pm 0.4) \times 10^{14}$ M$_\odot$, estimated by Giacintucci et al. (2017) using the T_X/M_{500} relation of Vikhlinin et al. (2009). This is relatively low mass for known mini-halo clusters – for example, it is the second-least-massive cluster in the sample of Giacintucci et al. (2019). We do, however, note some discrepancy in the literature regarding the cluster mass: Rossetti et al. (2017) derive a much greater value of $M_{500} = 7 \times 10^{14}$ M$_\odot$ using the L_X/M_{500} of Pratt et al. (2009). The central entropy for MS 1455.0 + 2232 is 16.88 keV cm^2 (Cavagnolo et al. 2009).

The mini-halo in MS 1455.0+2232 was first reported by Venturi et al. (2008) using 610 MHz observations performed with the Giant Metrewave Radio Telescope (GMRT; Swarup 1990). Venturi et al. (2008) identified it as a 'core-halo' structure, measuring a largest angular size of around 90 arcsec (347 kpc with our cosmology). More recently, Giacintucci et al. (2019) present a re-analysis of archival narrow-band 1.4 GHz Very Large Array (VLA) A- and C-configuration observations. The mini-halo is only partially resolved in their C-configuration image, and appears less extended (∼60 arcsec in diameter, or 231 kpc with our cosmology) than at lower frequencies. Giacintucci et al. (2019) estimate a spectral index of $\alpha^{1.4\ \mathrm{GHz}}_{610\ \mathrm{MHz}} = -1.45 \pm 0.22$.

2 OBSERVATIONS & DATA REDUCTION

2.1 Radio: MeerKAT

MS 1455.0+2232 was observed with the MeerKAT telescope on 2021 April 25 (SB 20210301-0026). Observations were performed using the L-band receivers, with 4096 channels covering a frequency range 872–1712 MHz. Following standard MeerKAT practice, bandpass calibrators were observed roughly every 3 h during the observing run. These were the bright radio sources PKS B0407−658 and PKS B1934−638, the latter of which was also used to set the absolute flux density scale. The compact radio source J1445+0958 was observed for 2 min at a half-hour cadence to provide an initial calibration of the time-varying instrumental gains. The total integration time on MS 1455.0+2232 was 5.5 h.

To calibrate the electric vector position angle, we included two 5-min scans on the known polarization calibrator 3C 286, separated by a broad parallactic angle range. While mini-haloes are expected to be largely depolarized, no statistical study of their polarization properties has been performed to date. We will examine the polarization properties of our full sample of mini-haloes (as well as radio sources of interest in the wider field) in future works.

Initial calibration and flagging was performed using the Containerized Automated Radio Astronomy Calibration (CARACAL) pipeline[2] (Józsa et al. 2020, 2021), which uses the Stimela framework (Makhathini 2018) as a wrapper around standard Common Astronomy Software Application (CASA) calibration tasks. We used `CARACal` to perform full-polarization calibration, although this paper details exclusively radio continuum results.

The `CARACal` pipeline also incorporates various flaggers. During pipeline execution, we flagged shadowed antennas, as well as specific channel ranges corresponding to the MeerKAT bandpass edges and bands that are known to be dominated by radio frequency interference (RFI). We also applied automatic sum-threshold flagging to our calibrator data using the `tfcrop` algorithm. After a first pass through flagging and initial calibration, we re-flagged our data using `tfcrop` before re-deriving all calibration tables – delays, bandpass, parallel-hand and cross-hand gains, and instrumental leakage – to refine our solutions, before applying these calibration tables to our target.

An initial round of flagging was performed on our target visibilities using the `Tricolour` flagger[3] (Hugo et al. 2021, in press) to execute a first (relatively shallow) pass of automated sum-threshold flagging within `CARACal`. We then generated an initial sky model using `DDFacet` (Tasse et al. 2018), which was subtracted from our data before running a second pass of `Tricolour` flagging on the residual data. Finally, we averaged our data by a factor of 8 in frequency, yielding 512 output channels of 1.67 MHz width, before proceeding to self calibration.

All self calibration was carried out using the KILLMS software package (`kMS`; Tasse 2014; Smirnov & Tasse 2015). We performed three rounds of direction-independent (DI) phase-only self calibration and two rounds of DI amplitude-and-phase self calibration. Imaging was again performed with `DDFacet` using `robust` =−0.5 weighting (Briggs 1995) in order to achieve a balance between resolution, signal-to-noise, and sensitivity to diffuse radio emission.

[2] https://github.com/caracal-pipeline/caracal
[3] https://github.com/ska-sa/tricolour

Downloaded from https://academic.oup.com/mnras/article/512/3/4210/6547010 by guest on 07 March 2025

We used the sub-space deconvolution (Tasse et al. 2018) algorithm in order to more accurately reconstruct the emission from the various resolved radio sources across the field of view. After five rounds of DI self-calibration, our solutions had largely converged, and we inspected our image for residual direction-dependent (DD) errors.

Throughout the self-calibration process, we used a quality-based weighting scheme (see Bonnassieux et al. 2018 for details) to weight our calibration solutions. This scheme makes use of gain statistics to estimate the relative quality of each solution, and weight each corrected visibility accordingly. In general, this results in faster self-calibration convergence. These weights are computed by default by `kMS` after each solve, as minimal computational overhead is required.

While we had achieved a generally high dynamic range after DI self-calibration, we noted some residual DD errors in the wider field. To correct for these, we tessellated the sky into 16 directions and performed two rounds of DD calibration, applying gains in both amplitude and phase during each imaging step. Once no further improvement was achieved from our self-calibration process, we generated an 'extracted' data set covering the immediate region around MS 1455.0+2232 by subtracting our best sky model of all sources more than 0.2° from the cluster. MeerKAT has a large field of view at L-band: the primary beam full width at half-maximum (FWHM) is ∼67 arcmin at 1.28 GHz; (Mauch et al. 2020). As our target occupies a small fraction of this field of view, the extraction step allowed us to re-image our target with different weighting schemes and *uv*-selection ranges with manageable computational overhead.

2.2 Radio: LOFAR

MS 1455.0+2232 was observed with LOFAR as a part of the LOFAR Two-Metre Sky Survey (LoTSS; Shimwell et al. 2017). The nearest field centre (P225+22; 0.81° separation) was observed using the full International LOFAR Telescope (ILT; van Haarlem et al. 2013) in `HBA_DUAL_INNER` mode for a total of 8 h on 2020 May 3. These data cover the frequency range 120–169 MHz.

2.2.1 Dutch LOFAR array

The data from the Dutch LOFAR array (Core and Remote stations, encompassing baselines out to ∼80 km) were processed using the LoTSS pipeline.[4] The pipeline steps are discussed in depth by Shimwell et al. (2017, 2019) and Tasse et al. (2021); however, in brief, this pipeline performs flagging, initial calibration, and both DI and DD self calibration using `killMS` and `DDFacet`. Following pipeline processing, an 'extracted' data set was created (for details of the extraction process, see van Weeren et al. 2021) containing the region around MS 1455.0+2232.

2.2.2 International LOFAR telescope

LoTSS observations are performed with the full ILT as standard, providing access to sub-arcsec resolution images at 145 MHz. To perform the calibration using the complete LOFAR array, we first used the PREFACTOR software package (van Weeren et al. 2016; Williams et al. 2016; de Gasperin et al. 2019) to calibrate the Dutch part of the array. Following initial RFI flagging, a model of the calibrator source (3C 196) was used to correct for the polarization alignment, Faraday rotation, bandpass, and finally clock offsets. With these calibration solutions applied to the data, a single phase-only cycle of self calibration was performed on the Dutch stations using a sky model obtained from the first Alternative Data Release of the TIFR-GMRT Sky Survey (Intema et al. 2017). Afterwards, the long-baseline pipeline discussed by Morabito et al. (2022) was employed to calibrate the international stations for ionospheric dispersive delays using a bright and compact source from the Long Baseline Calibrator Survey (Jackson et al. 2016, 2022). These calibration solutions were transferred to the target source and applied to the data. To solve for the residual dispersive delay errors due to direction dependence of this effect, a final long-interval self-calibration routine is performed on a nearby source instead of the target source, due to the faintness of the target.

2.3 Radio: ancillary data

MS 1455.0+2232 has previously been observed with the GMRT using the legacy GMRT Software Backend (GSB) at 610 MHz, with 32 MHz bandwidth. Observations were carried out on 2005 October 03, for a total of 166 min on-source time. These observations were first published by Venturi et al. (2008) and have subsequently been used by other authors (Mazzotta & Giacintucci 2008; Ignesti et al. 2020). We re-processed the raw visibilities from these observations using the Source Peeling and Atmospheric Modelling (`SPAM`; Intema et al. 2009) pipeline in a fully automated manner, as described by Intema et al. (2017).

We also sourced a 3 GHz mosaic image of MS 1455.0+2232 from the first two epochs of the Karl G. Jansky VLA Sky Survey (VLASS; Lacy et al. 2020) via the Canadian Initiative for Radio Astronomy Data Analysis (CIRADA) image cutout server. Finally, we searched the VLA data archive for historic VLA data sets covering MS 1455.0+2232. We retrieved observations at 1.4, 4.85, and 8.46 GHz from projects AE117 (performed 1998 April 12), AE125 (performed 1999 January 16), and AE317 (performed 1994 March 12). These data sets were reduced using standard techniques in CASA v6.1.2.7. All ancillary data sets used in this work provide relatively limited sensitivity to the diffuse emission of the mini-halo, and thus their use was restricted to providing flux density measurements for the radio counterpart to the BCG. We do not present images from these archival data sets in this manuscript.

2.4 Radio: post-processing

After calibration, we used WSCLEAN (Offringa et al. 2014; Offringa & Smirnov 2017) version 2.10.0[5] to generate science-quality images from our extracted MeerKAT and LOFAR data sets, to ensure that no discrepancies were introduced by the use of different algorithms.

When imaging with `WSclean`, we employed multiscale clean in order to optimally recover diffuse radio emission. The `-auto-mask` and `-auto-threshold` functionality was used to automate the deconvolution process; with the well-filled *uv*-plane of both our deep LOFAR and MeerKAT observations, each data set has a well-behaved point-spread function (PSF) with low-level sidelobes, and no significant spurious components were picked up by the auto-masked cleaning.

Given the large fractional bandwidth of both LOFAR and MeerKAT, we cleaned using the `-join-channels` and `-channels-out` options to improve the wide-band deconvolution. Stokes *I* images were produced in 6 (24) sub-bands across the

[4] github.com/mhardcastle/ddf-pipeline/

[5] WSclean is available at https://gitlab.com/aroffringa/wsclean

Downloaded from https://academic.oup.com/mnras/article/512/3/4210/6547010 by guest on 07 March 2025

LOFAR HBA (MeerKAT) bandwidth, in addition to multifrequency-synthesis images at frequencies of 145 MHz for LOFAR and 1283 MHz for MeerKAT. We also employed an inner *uv*-cut of 80λ to exclude baselines between the two substations of each LOFAR HBA Core Station; to ensure a consistent maximum recoverable angular scale, we adopted the same inner *uv*-cut for our MeerKAT imaging.

We then performed a further single round of DI self-calibration on our MeerKAT data using the LOFAR Default Pre-Processing Pipeline (van Diepen, Dijkema & Offringa 2018), solving for a full-Jones gain matrix. Further self calibration did not yield appreciable improvement; similarly, further self calibration of our extracted LOFAR data set yielded no improvement in image quality. As such, we concluded that our calibration had converged and proceeded to create our final images.

Representative low- and high-resolution images were produced by varying the `robust` parameter between different `WSclean` imaging runs. We used `robust` $=-0.5$ for low-resolution imaging and `robust` $=-2.0$ (corresponding to `uniform` weighting) for high-resolution imaging.

2.4.1 Flux scaling

The MeerKAT data presented in this work had the flux density scale set using observations of PKS B1934−638, tied to the Reynolds (1994) scale, which is itself tied to the Baars et al. (1977) scale. Observations with LOFAR are tied to the Scaife & Heald (2012) flux scale. The flux scale of all ancillary VLA data sets used in this work was set using the Baars et al. (1977) scale. The archival GMRT data were processed using the `SPAM` pipeline, which uses the Scaife & Heald (2012) scale, so no conversion is required. When defining their flux scale, Scaife & Heald brought all measurements for their selected calibrator sources on to the Roger, Costain & Bridle (1973) scale, which is consistent with the Kellermann (1966) scale above 325 MHz.

Table 7 of Baars et al. (1977) presents a set of factors for the ratio of their scale to other flux scales, including the Kellermann (1966) scale. Thus, we used a polynomial fit to these ratios (performed in log-linear space) to derive the scaling factor required to bring our MeerKAT images into consistency with the LOFAR flux scale. The required conversion factor at the reference frequency of our MeerKAT observations ($\nu_{\rm ref} = 1283$ MHz) yielded by our polynomial fit was 0.968. We note that for all frequencies considered in this work, our nth-order polynomial fits converged to broadly consistent values for $4 \leq n \leq 10$; any error induced by imprecise flux scale conversion is thus small compared to the overall flux scale and measurement uncertainties.

To verify the flux scale of our LOFAR data set, we used `WSclean` to generate an image at 6 arcsec resolution. This image was then compared with the well-verified flux density scale of LoTSS. This step involves extracting a catalogue from the target field, using the Python Blob Detection and Source Finder software (PYBDSF; Mohan & Rafferty 2015). The catalogue is then compared with the catalogue derived from the full-field LoTSS image, and filtered to select only compact sources with a signal-to-noise ratio at least seven. Finally, this routine performs a linear regression best-fitting in the flux:flux plane in order to derive the bootstrap factor. The application of this technique is discussed in detail by Hardcastle et al. (2016) and Shimwell et al. (2019). For our extracted LOFAR data set, we require a bootstrap factor of 1.0899 to align with the LoTSS flux scale; for the full ILT image, we require a bootstrap factor 1.149. We adopt a typical 5 per cent uncertainty in the flux scale of our MeerKAT images; following Shimwell et al. (2022), we also adopt a representative 10 per cent uncertainty for the flux scale of our LOFAR images.

2.4.2 Source subtraction and final imaging

Several compact or partially resolved sources are visible in the region of the mini-halo in MS 1455.0+2232, including the compact radio source associated with the BCG (see Fig. 1). To extract the clean components for these sources, we imaged again with `WSclean`, applying an inner *uv*-cut of 5kλ (corresponding to a spatial scale of 41 arcsec or a linear scale of 158 kpc) to filter the diffuse emission of the mini-halo. This scale was chosen as it effectively suppressed the mini-halo without reducing sensitivity to compact sources within the boundary of the diffuse emission, allowing us to subtract the true contaminating compact source flux. The recovered clean components corresponding to both the BCG, as well as sources in the vicinity of the mini-halo, were then subtracted. Finally, we generated source-subtracted images using `WSclean` with the settings described in Section 2.4 to produce maps at two different resolutions: a 'low-resolution' source-subtracted image at 15 arcsec resolution (using `robust` $=-0.5$) and a 'full-resolution' source-subtracted image at 8 arcsec resolution (using `robust` $=-1.0$). In each case, we used a combination of appropriate *uv*-tapering and subsequent image-plane smoothing to achieve the desired target resolution. We applied a Gaussian *uv*-taper of 6 and 12 arcsec before convolving the final images to our target resolution of 8 and 15 arcsec, respectively.

2.5 X-ray: *Chandra*

We reanalysed the archival *Chandra* ObsID 4192 of MS 1455.0+2232 originally presented in Mazzotta & Giacintucci (2008). The observation took place on 2003 September 5 (PI Mazzotta) is 95 ks long, and used *Chandra* ACIS-I in VFAINT mode placing the cluster in the I3 chip. Data were processed from the `level = 1` event file using CIAO V4.13 with CALDB V4.9.0. We searched for time periods affected by soft proton flares by inspecting the light curve extracted in the 0.5–7.0 keV band from the S2 chip that was kept on during the observation. The net time obtained after removing such periods is 88.6 ks. To maximize the signal-to-noise ratio from the ICM emission, exposure corrected images were created in the 0.5–2.0 keV energy band. Point sources were detected with the `wavdetect` task, visually inspected, and removed from the image by replacing them with random values extracted from neighbouring pixels.

We produced projected temperature and entropy maps of the ICM performing spectral analysis in regions defined by CONTBIN V1.5 (Sanders 2006). This algorithm allows us to bin regions of the image with similar surface brightness, and is particularly suited to studying the spatial variations of the thermodynamic quantities in galaxy clusters. During the binning process, we required that each spectral region had at least 1000 net counts in the 0.5–7.0 keV band. Thus, spectral extraction and fitting were performed with XSPEC V12.10.0c (Arnaud 1996). Following Botteon, Gastaldello & Brunetti (2018), we accounted for the X-ray background by modelling the spectrum extracted from a region in the ACIS-I field-of-view free from the cluster emission, adopting an astrophysical and an instrumental component. The former is due to thermal emission from the galactic halo and local hot bubble plus the contribution of the unresolved emission from distant point sources, whereas the latter is due to

Downloaded from https://academic.oup.com/mnras/article/512/3/4210/6547010 by guest on 07 March 2025

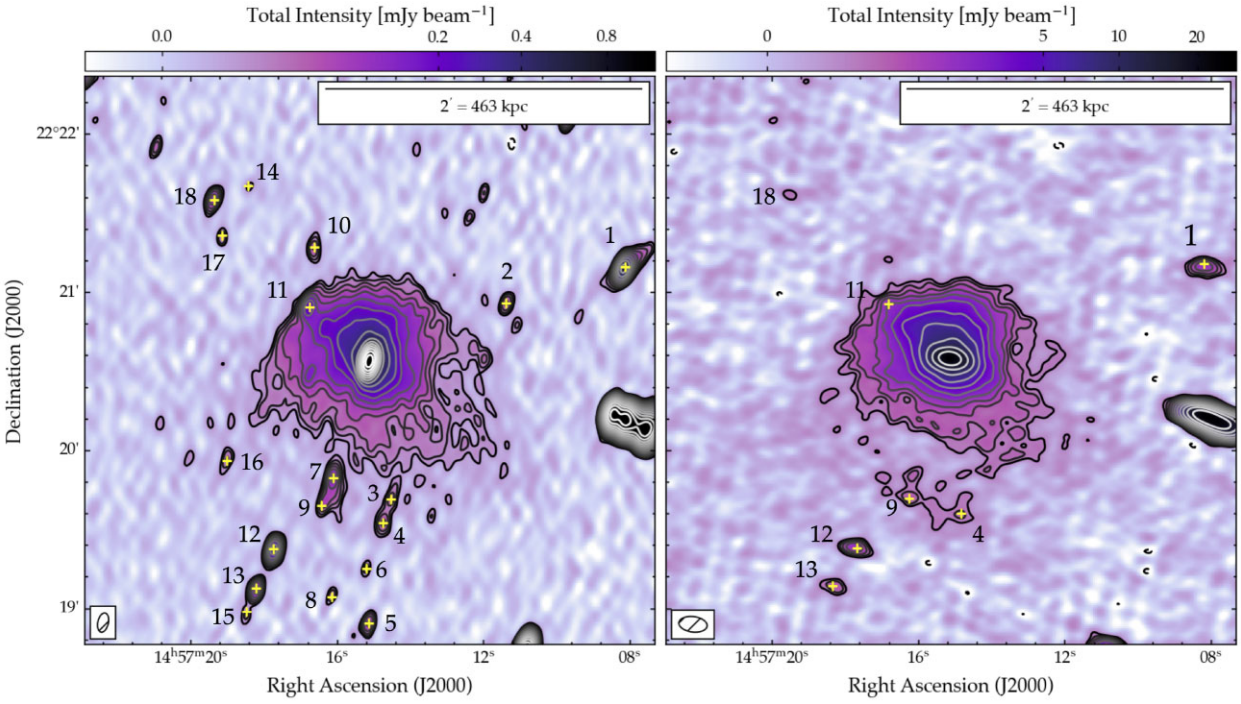


Figure 2. Radio continuum images of MS 1455.0+2232 with MeerKAT at 1283 MHz (*left*) and LOFAR HBA at 145 MHz (*right*) produced using `robust` =−0.5. Image properties (resolution and rms noise) are listed in Table 1; the restoring beam is indicated by the hatched ellipse in the lower-left corner of each subplot. Contours start at 4σ and scale by a factor $\sqrt{2}$. The −4σ contour is also shown by dashed lines. Yellow plus signs (' + ') denote sources (other than the BCG) that were modelled and subtracted from each data set; see online supplementary material for flux density measurements and cross-identifications.

Table 1. Summary of image properties. A '(sub)' indicates source-subtracted radio images. 'LOFAR ILT' refers to our image made using the full ILT.

Telescope	`Robust`	RMS noise (μJy beam^{-1})	Resolution (arcsec × arcsec)	PA (deg)
LOFAR	−0.5	140	10.8 × 5.8	+83
	−2.0	829	3.9 × 2.7	+103
LOFAR (sub)	−0.5	159	15 × 15	+0
	−1.0	179	8 × 8	+0
MeerKAT	−0.5	5.9	7.4 × 4.0	+168
	−2.0	19.8	5.5 × 2.7	+170
MeerKAT (sub)	−0.5	8.0	15 × 15	+0
	−1.0	7.7	8 × 8	+0
LOFAR ILT	+0.5	66.3	0.55 × 0.30	+6

the interaction of high-energy particles with the instrument, which was modelled using the analytical model of Bartalucci et al. (2014). We adopted a thermal plasma to model the ICM emission, leaving the normalization, metallicity, and temperature as free parameters. Projected values of entropy (K) were obtained combining the best-fitting temperature (kT) with the emission measure (EM) as $K = kT \times \mathrm{EM}^{-1/3}$. In the fitting, we adopted the abundance table from Asplund et al. (2009) and the column density $N_{\mathrm{H}} = 3.60 \times 10^{20}$ cm^{-2} (Willingale et al. 2013).

3 RESULTS

3.1 Radio continuum properties

Fig. 2 presents our MeerKAT and LOFAR images of MS 1455.0+2232 prior to source subtraction, imaged using `robust` =−0.5. The sensitivity and resolution of these images is presented in Table 1. With the excellent sensitivity afforded by our observations, the mini-halo in MS 1455.0+2232 is recovered at high signal to noise at both 1283 and 145 MHz. We also identify multiple compact and extended sources in the wider field, including a likely cluster-member head-tail radio galaxy to the West of the mini-halo (see also Fig. 1).

As is visible in Figs 1 and 2, the mini-halo itself is asymmetric at both 1283 and 145 MHz, appearing generally brighter to the north of the cluster centre (where we find the compact radio source associated with the BCG) with more extended fainter emission trailing towards the south and south-west. This fainter emission to the south and south-west has not been conclusively reported in previous radio studies at comparable resolution (Mazzotta & Giacintucci 2008; Venturi et al. 2008; Giacintucci et al. 2019) although we note a tentative detection at low resolution (∼15 arcsec) by Venturi et al. (2008).

However, as is visible in Fig. 2, there are multiple sources that lie in the vicinity of the mini-halo, or coincident with the diffuse emission. We aim to explore the diffuse radio emission from MS 1455.0+2232, and therefore excision of these contaminants is necessary. These were modelled and subtracted as discussed in Section 2.4.1; the sources that were subtracted (aside from the BCG) are identified by yellow plus-signs (' + ') in Fig. 2. Flux density measurements for these sources, along with SDSS cross-identifications and redshifts, are presented in the online supplementary material.

3.1.1 Source-subtracted images

Fig. 3 presents our source-subtracted, *uv*-tapered images of MS 1455.0+2232 at 8 arcsec resolution (*top row*) and 15 arcsec resolution (*bottom row*). With the enhanced sensitivity to very low

Downloaded from https://academic.oup.com/mnras/article/512/3/4210/6547010 by guest on 07 March 2025

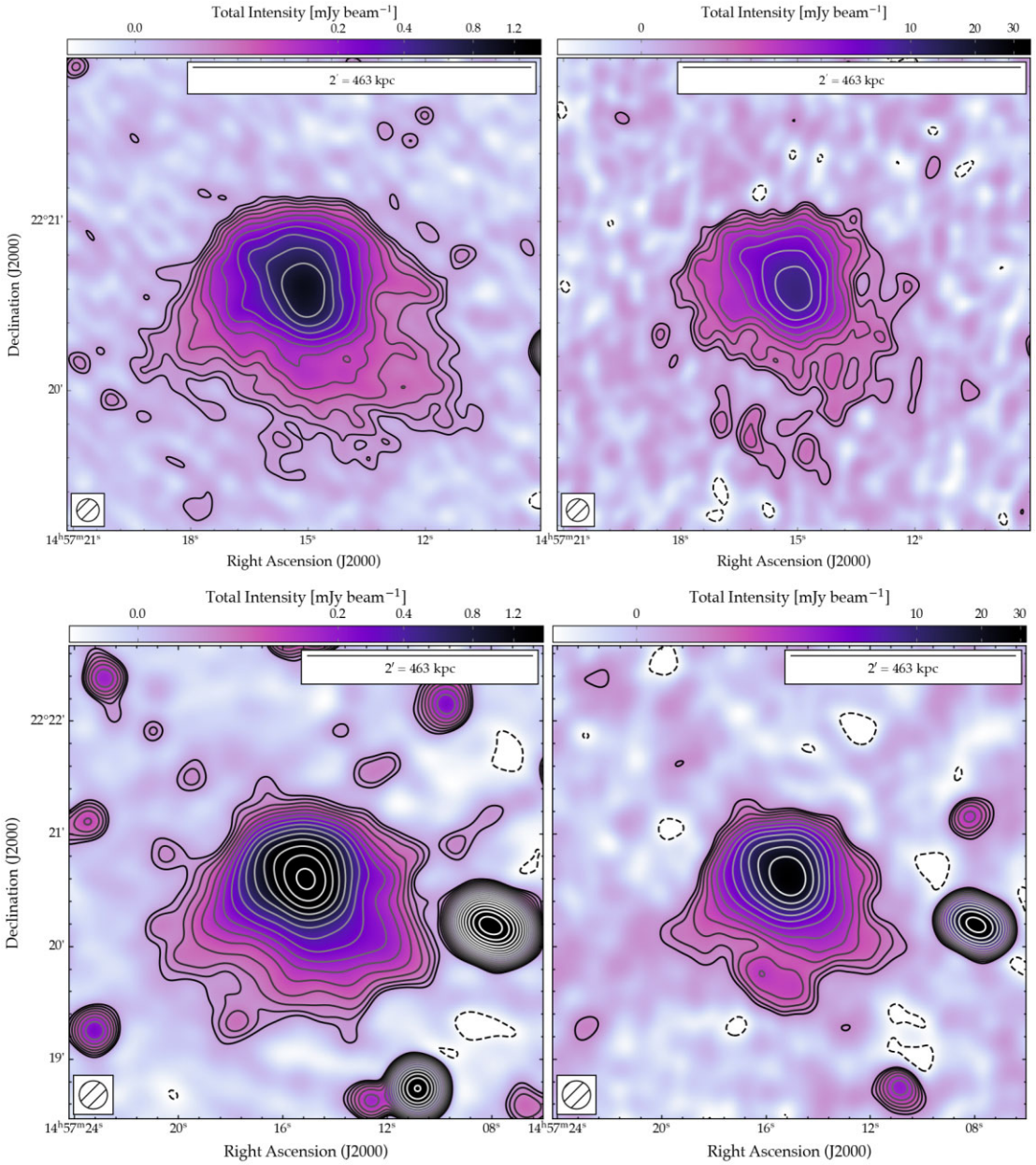


Figure 3. Source-subtracted images of MS 1455.0+2232 at 1283 MHz (MeerKAT; *left*) and 145 MHz (LOFAR; *right*), shown at 8 arcsec resolution (*top*) and 15 arcsec resolution (*bottom*). Contours are shown at intervals of $\sqrt{2}$ starting from 3σ, where the values of σ are listed in Table 1; the -3σ contour is shown as a dashed line. The colour scale ranges from -3σ to 200σ and is shown on an arcsinh stretch to emphasize diffuse emission. The scale bar denotes the linear size at $= 0.258$ corresponding to an angular scale of 2 arcmin.

surface brightness radio emission, the diffuse radio emission of the mini-halo is detected to a much greater extent. From our 15 arcsec resolution MeerKAT image at 1283 MHz, we measure a largest angular scale of 152 arcsec, corresponding to a largest linear size (LLS) of 586 kpc with our cosmology. This is 69 per cent larger than previously reported by Venturi et al. (2008) at 610 MHz, who measured a LAS (LLS) of 90 arcsec (347 kpc with our cosmology). At 145 MHz, the LAS is 122 arcsec (471 kpc).

We note that it is unusual to find non-thermal cluster phenomena that are more extended at higher frequencies than lower frequencies. The faint, steep-spectrum radio sources often associated with clusters typically trace weak and/or inefficient (re-)acceleration processes in the ICM, and are more commonly found to decrease in size with increasing frequency (reflecting the nature of the acceleration mechanism, e.g. Rajpurohit et al. 2021a,b). However, our MeerKAT images achieve a very low rms noise of 7.3 μJy beam^{-1} at 1283 MHz; as such, a source that has a 1σ flux density at each frequency would have a spectral index of $\alpha = -1.37$. This means that the larger extent at higher frequencies does not necessarily imply a spectral flattening.

3.2 X-ray properties

Fig. 4 shows the X-ray surface brightness measured by *Chandra* in the 0.5–2.0 keV band, as well as several quantities derived from our X-ray data. These are the ICM temperature (panel b), X-ray surface brightness gradient (panel c), and ICM entropy (panel d).

Downloaded from https://academic.oup.com/mnras/article/512/3/4210/6547010 by guest on 07 March 2025

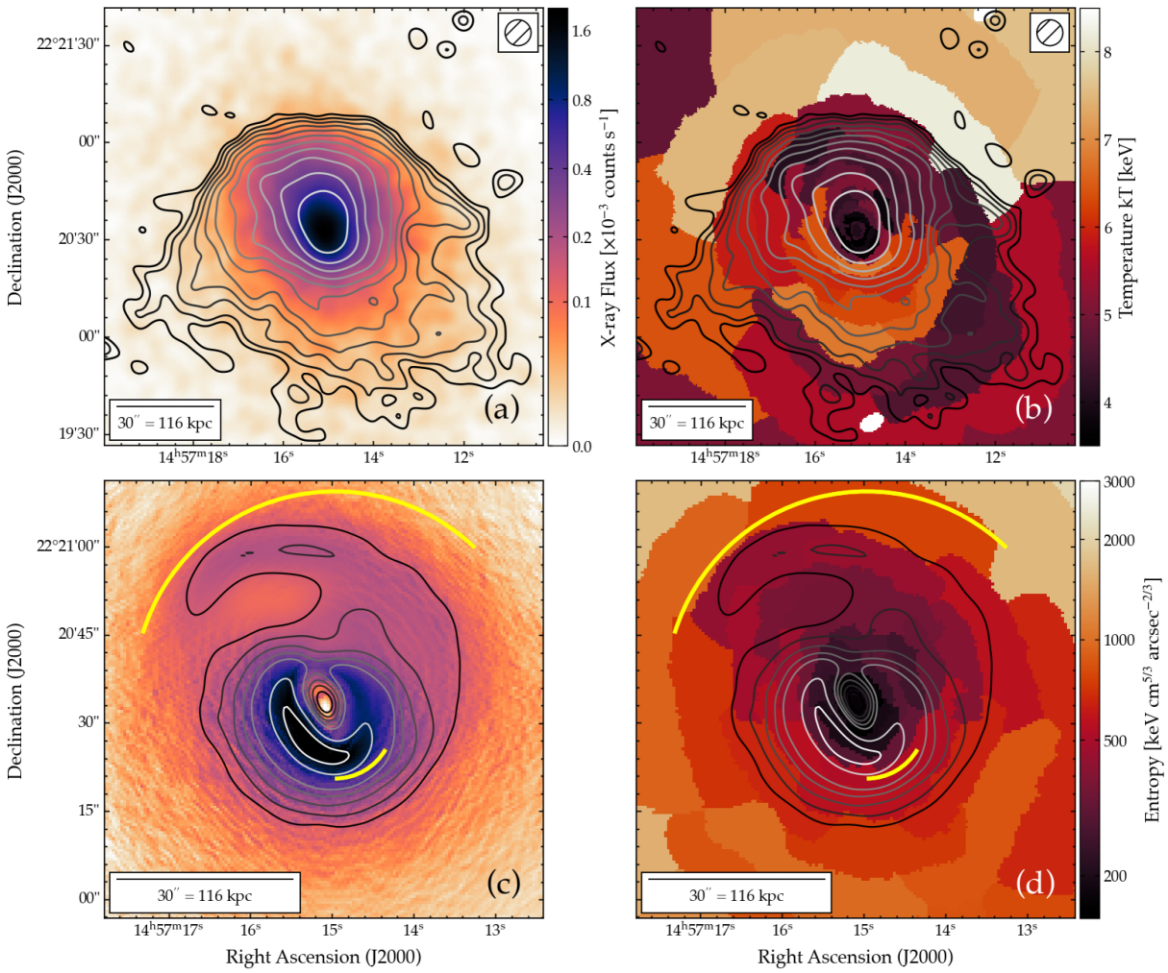


Figure 4. Multiwavelength images of MS 1455.0+2232. Background colourmaps show different quantities derived from our *Chandra* data: (a) 0.5–2.0 keV X-ray flux, smoothed with a Gaussian of 8 arcsec FWHM, (b) ICM temperature, (c) X-ray surface brightness gradient, (d) ICM entropy. In panels (a) and (b), contours show 1283 MHz surface brightness measured by MeerKAT at 8 arcsec resolution as per Fig. 3 (the resolution is shown by the hatched circle in the upper-right corner). Contours in panels (c) and (d) denote the X-ray gradient, smoothed with a Gaussian of FWHM 3 pixels, with levels chosen to highlight the structure of the sloshing spiral. Yellow arcs trace the cold fronts identified by Mazzotta et al. (2001a); our new analysis reveals that these trace features visible in the larger-scale sloshing spiral. The bright 'hotspot' at the centre of the sloshing spiral is clearly visible at the centre of panel (c).

The X-ray gradient map is particularly useful to highlight the surface brightness discontinuities in the ICM, such as shocks and cold fronts, and study their connection with the radio emission. The map shown Fig. 4 panel (c) was obtained using the adaptively smoothed Gaussian Gradient Magnitude filter recently introduced by Sanders et al. (2021). This method adds in quadrature the gradients computed along the x- and y-axes from the $\log_{10}$ value of an adaptively smoothed X-ray image of the cluster (for MS 1455.0+2232, we adopted a smoothing signal-to-noise ratio of 25). Our image clearly shows a spiral-like structure that is often associated with core-sloshing in relaxed clusters: a sloshing spiral (see for example Sanders et al. 2016a, b; Werner et al. 2016; Douglass et al. 2018).

The sloshing spiral is asymmetric around its peak (which is traced by the 'hotspot' in Fig. 4, panel c): it occupies an elliptical region 66 × 60 arcsec (at PA ∼29°) centred on (J2000 RA, Dec.; $14^{h}07^{m}5.^{s}14$, $+22°20'37''.6$). This corresponds to a physical scale of 254 × 232 kpc. Our new analysis reveals that the cold fronts previously identified by Mazzotta & Giacintucci (2008) form a part of the larger spiral structure in MS 1455.0+2232; this kind of structure almost perfectly matches prototypical core-sloshing spirals seen in numerical simulations (e.g. Ascasibar & Markevitch 2006; ZuHone et al. 2013).

Panel (d) of Fig. 4 shows the (projected) entropy derived from our *Chandra* data. We highlight that the low-entropy regions seen in panel (d) closely follow the boundaries of the sloshing spiral, suggesting that low-entropy gas is being disturbed by the core sloshing. Indeed, these kind of structures have been observed in sloshing clusters (Fabian et al. 2006; Ghizzardi, De Grandi & Molendi 2014) and are also predicted by numerical simulations (Ascasibar & Markevitch 2006; ZuHone et al. 2013). The simulations by Ascasibar & Markevitch (2006) in particular suggest that this kind of sloshing structure can be generated by minor or off-axis merger events. While there is no evidence of substructure in the galaxy distribution of MS 1455.0+2232 that might indicate a minor merger, to the best of our knowledge such an investigation has not been performed to date, and is beyond the scope of this paper.

Fig. 5 presents multiwavelength images of MS 1455.0+2232, showing the X-ray surface brightness measured by *Chandra* (smoothed with a Gaussian of 15 arcsec FWHM) and radio contours from our source-subtracted MeerKAT and LOFAR data at 15 arcsec

Downloaded from https://academic.oup.com/mnras/article/512/3/4210/6547010 by guest on 07 March 2025

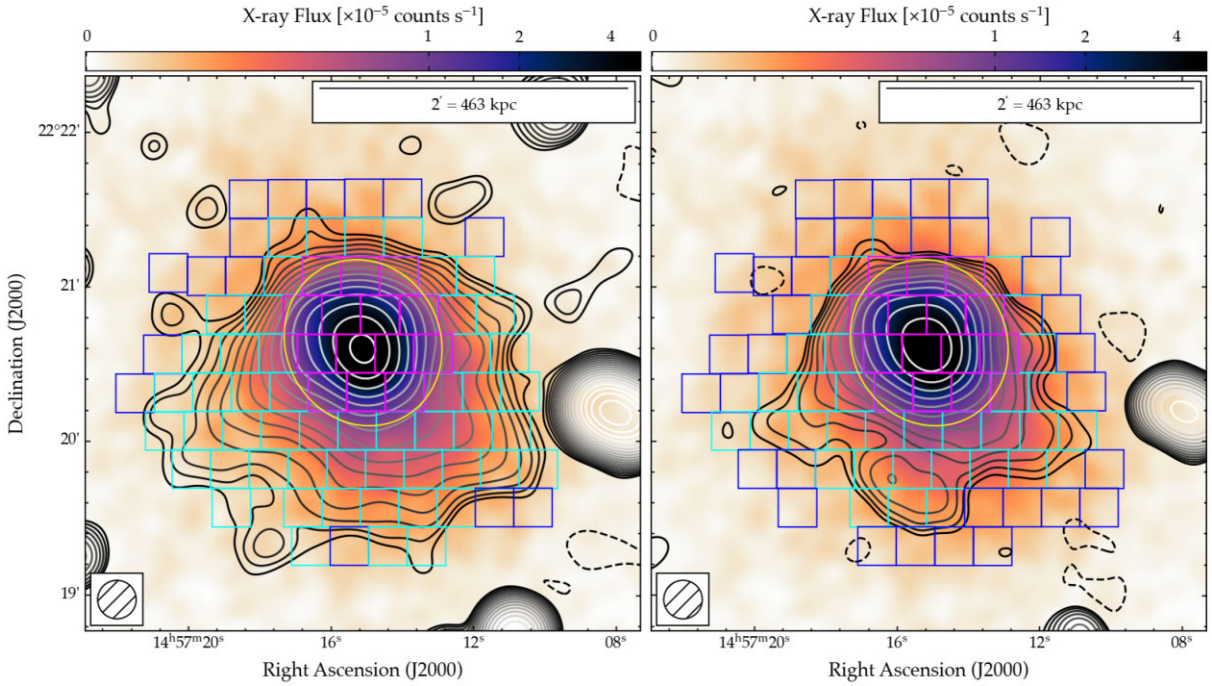


Figure 5. Multiwavelength images of the mini-halo in MS 1455.0+2232. Colour map shows the X-ray surface brightness measured by *Chandra* in the 0.5–2 keV band, smoothed with a 15 arcsec FWHM Gaussian to match the resolution of our radio data. Contours denote the source-subtracted radio data (*left*: MeerKAT; *right*: LOFAR) at 15 arcsec resolution, starting at 3σ and scale by $\sqrt{2}$, as per Fig. 3. Boxes show the regions used to profile the radio/X-ray correlations, with magenta boxes indicating regions within the boundary of the sloshing spiral (identified by the yellow ellipse), cyan boxes indicating regions outside the sloshing spiral, and blue boxes indicating regions where the average radio surface brightness is below the corresponding 3σ level.

resolution overlaid to guide the reader. We also trace the outer edge of the sloshing spiral identified in Fig. 4. Finally, Fig. 5 also shows boxes which will be later used to study point-to-point correlations between thermal and non-thermal properties, as well as profiling the spectral index.

From Fig. 5, the mini-halo in MS 1455.0+2232 extends far beyond the boundaries of the sloshing spiral: the diffuse synchrotron emission fills almost the entire X-ray-emitting region (above a count rate of 5×10^{-7} counts s^{-1}). To the north, the mini-halo extends for 20 arcsec (77 kpc) beyond the boundary of the sloshing spiral. However, to the south-east, south, and south-west, the mini-halo extends 56 arcsec (or 216 kpc) beyond the outer edge of the sloshing spiral, as traced by our MeerKAT data at 1283 MHz.

Many historic mini-halo studies have not detected significant radio emission outside of the sloshing regions in relaxed cool-core clusters. As such, most theoretical models that associate mini-haloes with turbulence predict that particle acceleration (and thus diffuse synchrotron emission) will be limited to the relatively small scales of the sloshing region (ZuHone et al. 2013). MS 1455.0+2232 has historically been one of the prototypical sloshing clusters where the mini-halo is believed to be generated by turbulence induced by core sloshing (Mazzotta & Giacintucci 2008), and thus the extent of the sloshing spiral and the diffuse mini-halo would appear to be in tension.

3.3 Radio emission from the brightest cluster galaxy

3.3.1 Integrated spectral energy distribution

To measure the flux density of the radio counterpart to the BCG, we used our uniform-weighted MeerKAT and LOFAR images with an inner *uv*-cut of 5 kλ. The BCG radio core remains unresolved at the resolution limit of these data (i.e. the core size is less than 2.6 arcsec or a physical scale of 10 kpc). We measure an integrated flux density of $S_{1283\,\mathrm{MHz}} = 4.74 \pm 0.24$ mJy from our MeerKAT image, and $S_{145\,\mathrm{MHz}} = 11.93 \pm 1.24$ mJy for the compact radio component detected in our uniform-weighted (`robust` $=-2$) LOFAR Dutch array map.

Thus, we find a two-point spectral index $\alpha^{145\,\mathrm{MHz}}_{1283\,\mathrm{MHz}} = -0.42 \pm 0.11$. This is significantly flatter than the spectral index previously reported by Giacintucci et al. (2019), who found $\alpha^{610\,\mathrm{MHz}}_{1.4\,\mathrm{GHz}} = -0.85 \pm 0.11$ (accounting for differences in spectral index convention). However, this previously reported spectral index is wholly tied to the calibration and deconvolution precision of both data sets.

Alongside our new MeerKAT and LOFAR observations, our reprocessing of archival narrow-band data sets provides the broad-band coverage necessary to explore the radio spectral energy distribution (SED) of the BCG. Table 2 lists the measurements from our new MeerKAT and LOFAR observations, as well as from our reprocessed ancillary data, plus a 28.5 GHz measurement with the Berkeley-Illinois-Maryland Association (BIMA) interferometer which is quoted directly from Coble et al. (2007). Fig. 6 presents the result of our analysis. The SED is well-characterized by a relatively flat-spectrum power-law between 145 MHz and 1.4 GHz, and exhibits departure from this power-law behaviour somewhere in the range 1.4 GHz to 3 GHz. We find a 610 MHz flux density of $S_{610\,\mathrm{MHz}} = 6.26 \pm 0.63$ mJy, measured from our final image produced by the `SPAM` pipeline. This is around 34 per cent lower than the value previously reported by Mazzotta & Giacintucci (2008); however, as is visible from Fig. 6 our newly measured 610 MHz flux density is entirely consistent with the overall SED profile.

Downloaded from https://academic.oup.com/mnras/article/512/3/4210/6547010 by guest on 07 March 2025

Table 2. Flux density measurements for the unresolved radio core of the BCG in MS 1455.0+2232. Note that all measurements are converted to the Scaife & Heald (2012) flux density scale, aside from the 28.5 GHz measurement which is quoted directly from Coble et al. (2007).

Frequency (GHz)	Flux density (mJy)
0.145	11.93 ± 1.24
0.610	6.26 ± 0.36
1.283	4.74 ± 0.24
1.4	4.56 ± 0.30
3.0	2.95 ± 0.32
4.85	2.27 ± 0.12
8.46	1.41 ± 0.08
28.5	0.96 ± 0.10

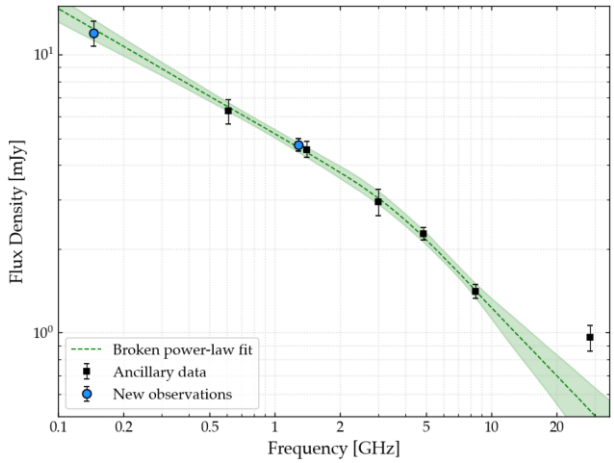


Figure 6. Radio SED for the compact radio source associated with the BCG in MS 1455.0+2232. Our new MeerKAT and LOFAR measurements at 1283 and 145 MHz are shown as blue circles; measurements from reprocessed archival data are shown as black squares. Dashed green line denotes our best-fitting broken power-law spectrum, with $\alpha_{\rm low} = -0.45 \pm 0.05$ below the break frequency ($\nu_{\rm b} = 3.12 \pm 1.35$ GHz) and $\alpha_{\rm high} = -0.81 \pm 0.18$ above the break; the green shaded region indicates the 1σ uncertainty explored by EMCEE. Note that the 28.5 GHz measurement was excluded from our fitting due to potential source variability at this frequency.

We modelled the behaviour of the SED using a broken power-law fit, and explored the uncertainty region using an 'affine invariant' Markov Chain Monte Carlo (MCMC) ensemble sampler (Goodman & Weare 2010) as implemented by the EMCEE package (Foreman-Mackey et al. 2013) to constrain the model. We note that the 28.5 GHz measurement was omitted from our fitting routine; the BIMA observations reported by Coble et al. (2007) were performed in the 1996–2002 period, and at these frequencies, variability on year-decade time-scales is likely. More recent observations at comparable frequency and resolution would be required to quantify this, however.

Our fitting routine yielded a best-fitting broad-band spectral index $\alpha_{\rm low} = -0.45 \pm 0.05$ below the break frequency, which is consistent with the two-point spectral index derived earlier. Above the break frequency, we find a best-fitting spectral index $\alpha_{\rm high} = -0.81 \pm 0.18$. The break frequency itself is poorly constrained by the available data: we find $\nu_{\rm b} = 3.1 \pm 1.4$ GHz. Further broad-band data from (for example) the VLA would be required to more accurately pinpoint the break frequency for this radio source.

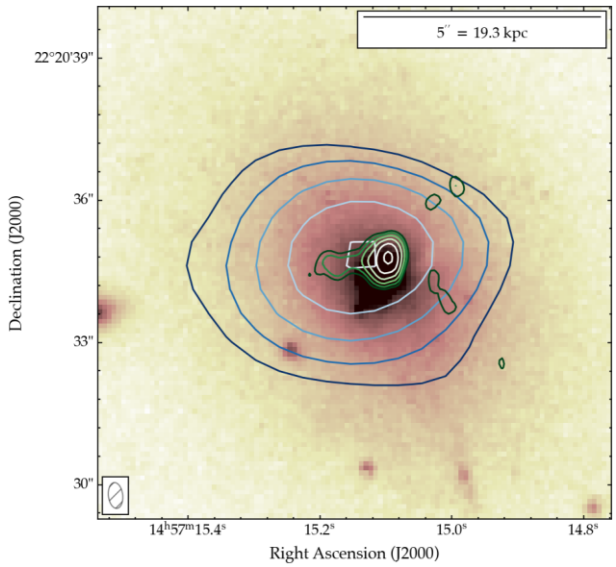


Figure 7. Multiwavelength zoom on the BCG of MS 1455.0+2232. The background colourmap shows a *Hubble Space Telescope* image taken with the Wide-Field and Planetary Camera 2 in the *F606W* filter. Blue contours show the `uniform`-weighted (`robust` −2) LOFAR surface brightness at a resolution of 3.9×2.7 arcsec^2; the first contour is at 4σ. Green contours show the radio surface brightness from our full ILT image at a resolution of 0.55×0.30 arcsec^2 (indicated by the hatched ellipse); the first contour is at 5σ. All contours increment by a factor of $\sqrt{2}$.

Given our spectral index convention, the *k*-corrected radio power is given by the following equation:

$$P_\nu = 4\pi\, D_{\rm L}^2\, S_\nu\, (1+z)^{-(1+\alpha)} \quad [{\rm W\ Hz^{-1}}] \qquad (1)$$

where $D_{\rm L} = 1259.7$ Mpc is the luminosity distance at the cluster redshift of $z = 0.258$, and S_ν is the flux density at frequency ν. From our broad-band SED fit, we find $S_{1.4\ {\rm GHz}} = 4.45 \pm 0.18$ mJy. Thus, equation (1) yields a radio luminosity of $P_{1.4\ {\rm GHz}}$ (BCG) $= (7.44 \pm 0.30) \times 10^{23}$ W Hz^{-1}.

This radio power is a factor 3.5 lower than the 'BCG steep' radio power at 1 GHz derived by Richard-Laferrière et al. (2020) from flux density measurements presented by Hogan et al. (2015). However, as noted in the supplementary material of Hogan et al. (2015), their 1.4 GHz measurement likely recovers 'more diffuse emission from the non-core component', which may reflect a partial detection of the mini-halo. As such, the radio power derived from our measurements is not directly comparable with previous values reported by Hogan et al. (2015) and Richard-Laferrière et al. (2020).

3.3.2 Sub-arcsec LOFAR images

When measuring the integrated flux of the mini-halo, the dominant source of contamination is the compact radio source associated with the BCG. Fig. 7 presents a zoom on the BCG of MS 1455.0+2232, overlaid with contours from our high-resolution LOFAR image (produced using the Dutch array), as well as our sub-arcsec resolution image produced using the full ILT.

From Fig. 7, we see that the radio source associated with the BCG of MS 1455.0+2232 remains compact at a resolution of the Dutch array (around 2.5 arcsec). It is only with the sub-arcsec imaging capability of the ILT that we are able to decompose this compact radio source into multiple components: a dominant western component that

Downloaded from https://academic.oup.com/mnras/article/512/3/4210/6547010 by guest on 07 March 2025

appears to be slightly misaligned with the BCG, and a much weaker component that extends to the east.

We measure a total flux density of $S_{145\,\mathrm{MHz}} = 11.93 \pm 1.24$ mJy for the compact radio component detected in our high-resolution LOFAR Dutch array map. From the ILT map, the primary (western) component presents as a marginally resolved radio source with a peak flux density $S_{145\,\mathrm{MHz}} = 1.72$ mJy beam^{-1}. Integrating above the 4σ contour of our ILT map, we find a total integrated flux density of $S_{145\,\mathrm{MHz}} = 6.77 \pm 0.70$ mJy for both components. As such, our ILT image is around 57 per cent flux-complete; a significant fraction of the (unresolved) flux of the radio core lies below the surface brightness sensitivity level of our present ILT image.

This relatively poor flux completeness of our ILT image, combined with the lack of higher-frequency maps capable of achieving the same resolution, means that we cannot yet determine the nature of these multiple components. Deeper observations with the ILT would increase our flux completeness and allow us to better understand the morphology of this source. Spectral information would be required to better understand the nature of these components, with further observations at complementary frequencies using instruments such as eMERLIN and/or lower-frequency LOFAR Low-Band Antenna (LBA) VLBI involving the NenuFAR station in superstation mode (e.g. Zarka et al. 2020; Bonnassieux et al. 2020).

3.3.3 Radiative age

The spectral behaviour of resolved radio galaxies can be used to determine their magnetic field and radiative age assuming that the energy budget is equally distributed between magnetic fields and relativistic particles.

Following equations (24) and (26) of Govoni & Feretti (2004), we derive the equipartition magnetic field by modelling the two components of the BCG as two spheres of radius 0.6 and 0.35 arcsec (as seen in our ILT map in Fig. 7), obtaining a volume of $\sim$62 kpc^3. We assume a filling factor $\Phi = 1$ and a proton-to-electron energy ratio $k = 1$. The synchrotron luminosity was derived from the flux density measured at 145 MHz in our ILT map. The BCG equipartition magnetic field is $B_{\mathrm{eq}} = 1$ μG.

Assuming the continuous injection model (CI; Pacholczyk 1970), where freshly injected particles compensate the radiative losses, it is possible to derive the radiative age of the source (τ_{s}) as:

$$\tau_{\mathrm{s}} = 1590 \frac{B^{0.5}}{(B^2 + B_{\mathrm{IC}}^2)\,[(1+z)\nu_{\mathrm{b}}]^{0.5}} \quad [\mathrm{Myr}]\,, \tag{2}$$

where B_{IC} is the equivalent magnetic field due to inverse Compton losses that depends on redshift as $B_{\mathrm{IC}} = 3.25(1+z)^2$ μG, B is the BCG magnetic field, while $\nu_{\mathrm{b}} = 3.1 \pm 1.4$ GHz is the break frequency of the SED. Taking the BCG magnetic field to be the equipartition magnetic field derived earlier (i.e. $B = B_{\mathrm{eq}} = 1$ μG), we obtain a radiative age of $\tau_{\mathrm{s}} \simeq 46 \pm 20$ Myr. We note that the dominant contribution to this uncertainty budget is the significant uncertainty in the break frequency.

4 ANALYSIS: THE MINI-HALO IN MS 1455.0+2232

4.1 Spectral properties

4.1.1 Integrated spectral properties

Integrating above the 3σ contour in the corresponding MeerKAT and LOFAR images of the mini-halo in Fig. 3, we find a total flux density recovered by MeerKAT of $S_{1283\,\mathrm{MHz}} = 18.7 \pm 0.9$ mJy. For LOFAR, we measure a total integrated flux density of $S_{145\,\mathrm{MHz}} = 154.5 \pm 15.6$ mJy. Thus, our integrated spectral index for the mini-halo in MS 1455.0+2232 is $\alpha_{1283\,\mathrm{MHz}}^{145\,\mathrm{MHz}} = -0.97 \pm 0.05$.

This is significantly flatter than was previously reported by Giacintucci et al. (2019) for this cluster: $\alpha_{1.4\,\mathrm{GHz}}^{610\,\mathrm{MHz}} = -1.46 \pm 0.22$. The cause of this difference is readily apparent when comparing our Fig. 3 with their fig. 15. Only the brightest central region of the mini-halo is recovered by the VLA C-configuration observations presented by Giacintucci et al. (2019); as such they recover an integrated 1.4 GHz flux density $S_{1.4\,\mathrm{GHz}} = 8.5 \pm 1.1$ mJy. Our deeper MeerKAT observations are far more sensitive to the low-surface-brightness regions of the mini-halo, and as such our integrated flux density is more than double the value recovered by Giacintucci et al. (2019).

Few well-studied examples of mini-halo spectra exist in the literature; however, the integrated spectral index we find for MS 1455.0+2232 is significantly flatter than the mini-haloes hosted by RX J1532.9+3021 ($\alpha = -1.20 \pm 0.03$), the Perseus cluster ($\alpha = -1.21 \pm 0.05$), and the Ophiuchus cluster ($\alpha = -1.56 \pm 0.04$) for example (Giacintucci et al. 2014).

On the other hand, our integrated spectral index is consistent with some known mini-haloes. The mini-haloes in Abell 2667 ($\alpha = -1.0 \pm 0.2$; Giacintucci et al. 2019), the Phoenix Cluster ($\alpha = -0.95 \pm 0.10$; Raja et al. 2020; Timmerman et al. 2021), and RX J1720.1+2638 ($\alpha = -0.99 \pm 0.03$; Biava et al. 2021) all show a similar integrated spectral index to MS 1455.0+2232. Deep observations at complementary frequencies would be required to explore the spectral properties of this mini-halo further. However, to search for the presence of a spectral break, higher-frequency observations would be required with instruments such as the VLA (S- and/or C-bands) or the MeerKAT S-band receiver system. Such observations could provide important evidence when attempting to differentiate between the particle acceleration mechanism at work in MS 1455.0+2232.

4.1.2 Mini-halo luminosity

Using our 1283 MHz integrated flux density measurement and our integrated spectral index, we can use equation (1) to estimate the mini-halo luminosity. Using the canonical cluster redshift of $z = 0.258$, we find $\mathrm{P}_{1.4\,\mathrm{GHz}}\,(\mathrm{MH}) = (3.24 \pm 0.16) \times 10^{24}$ W Hz^{-1}. Due to differences in the methodology and the measured spectral index, this figure is not directly comparable to the radio power measurements previously reported by Venturi et al. (2008) and Giacintucci et al. (2019). In any case, despite deriving a larger value, our radio power measurement is consistent with the broader mini-halo population, which typically exhibit $\mathrm{P}_{1.4\,\mathrm{GHz}}\,(\mathrm{MH}) \sim 10^{23} - 10^{25}$ W Hz^{-1} (van Weeren et al. 2019, and references therein).

When combined with the BCG radio power derived earlier – $\mathrm{P}_{1.4\,\mathrm{GHz}}\,(\mathrm{BCG}) = (7.44 \pm 0.30) \times 10^{23}$ W Hz^{-1} – we can examine where MS 1455.0+2232 now lies in known power scaling planes. Fig. 8 presents the $\mathrm{P}_{1.4\,\mathrm{GHz}}\,(\mathrm{BCG})/\mathrm{P}_{1.4\,\mathrm{GHz}}\,(\mathrm{MH})$ plane for known radio mini-haloes, using the sample presented by Giacintucci et al. (2019). We also add the mini-halo candidate recently reported by Norris et al. (2021) at 943 MHz in the Evolutionary Map of the Universe (EMU; Norris et al. 2011) Pilot Survey region, with measurements scaled to 1.4 GHz using canonical spectral index values $\alpha = -0.7$ for the BCG and $\alpha = -1$ for the mini-halo.

From Fig. 8, we see that our new results place the mini-halo in MS 1455.0+2232 towards the middle range of the scaling plane

Downloaded from https://academic.oup.com/mnras/article/512/3/4210/6547010 by guest on 07 March 2025

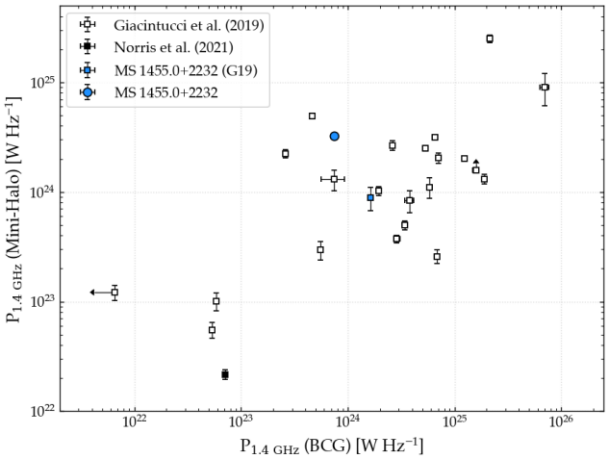


Figure 8. Power scaling plane for mini-haloes, showing how the mini-halo radio power, $P_{1.4\,GHz}$ (MH), scales with BCG radio power, $P_{1.4\,GHz}$ (BCG). Open squares denote known mini-haloes from the sample of Giacintucci et al. (2019), adjusted for differences in assumed cosmology; the black square denotes the mini-halo candidate recently reported by Norris et al. (2021). Blue points indicate the position of MS 1455.0+2232, with the square denoting the measurements from Giacintucci et al. (2019) and the circle indicating our new measurements (note that the uncertainties on our new measurements are not visible at this scale).

between mini-halo radio power and BCG radio power for the known population. However, we also see that our new measurements of the mini-halo and BCG radio power for this cluster have significantly shifted the position of MS 1455.0+2232 in this scaling plane, compared to the values reported by Giacintucci et al. (2019). We will revisit the scaling relation between $P_{1.4\,GHz}$ (MH) and $P_{1.4\,GHz}$ (BCG) in future for the full sample from our homogeneously selected mini-halo census.

4.1.3 Resolved spectral properties

Fig. 9 presents the map of the spectral index between 145 and 1283 MHz at both 8 and 15 arcsec resolution, as well as the associated uncertainty maps. From the upper panel of Fig. 9, we find a mean spectral index of $\langle\alpha\rangle = -1.07 \pm 0.10$ at 8 arcsec resolution. However, we see reasonably significant fluctuations in the observed spectral index, including some regions where the spectral index appears to steepen, particularly towards the north-eastern and southern/south-western extremes. To investigate the statistical significance of any overall spectral index steepening, we studied the spectral index behaviour both inside and outside the boundaries of the sloshing spiral.

Within the sloshing spiral boundary, we find $\langle\alpha_{in}\rangle = -1.03 \pm 0.08$; for regions outside the sloshing spiral, we find a slightly steeper spectral index of $\langle\alpha_{out}\rangle = -1.11 \pm 0.14$, although these are consistent at the 1σ level. Similarly, the standard deviation of spectral index is lower interior to the spiral ($\sigma_\alpha \sim 0.05$) than outside the spiral boundary ($\sigma_\alpha \sim 0.08$). We do note, however, that this comparison may be limited by small number statistics due to the relative sensitivity of our MeerKAT and LOFAR data.

Our lower-resolution (15 arcsec) spectral index map is presented in the lower panel of Fig. 9. While the mean spectral index of $\langle\alpha\rangle = -0.97 \pm 0.09$ is slightly flatter than the overall mean value, we find at 8 arcsec resolution, the two values are consistent to within 1σ. Overall, the spectral index across the majority of the mini-halo is largely uniform when observed at 15 arcsec resolution.

We repeated the comparison between the observed spectral index interior and exterior to the sloshing spiral at 15 arcsec resolution. As with our higher-resolution map, we find that the average spectral index is slightly steeper exterior to the spiral ($\langle\alpha_{out}\rangle = -1.0 \pm 0.10$) than interior ($\langle\alpha_{in}\rangle = -0.94 \pm 0.07$), although again these are consistent at 1σ. The standard deviation in spectral index is also a factor two greater exterior to the spiral ($\sigma_\alpha \sim 0.06$) than interior ($\sigma_\alpha \sim 0.03$).

Many of the steep-spectrum regions identified at 8 arcsec resolution appear less steep at 15 arcsec resolution – in particular, the steep-spectrum regions to the north-eastern and south-western edges of the mini-halo flatten slightly from $\alpha \sim -1.4$ to -1.1, which is more comparable with the overall profile. Given the surface brightness sensitivity limit of the available LOFAR data, we cannot currently determine whether the apparent steepening seen at 8 arcsec resolution is the result of signal-to-noise limits, or whether the slight flattening seen at 15 arcsec resolution is the result of blurring different regions with different spectral properties due to the broader PSF FWHM.

Towards the southernmost edge of the mini-halo, however, we find a relatively steep spectral index of $\langle\alpha\rangle = -1.45 \pm 0.18$ at 8 arcsec resolution and $\langle\alpha\rangle = -1.37 \pm 0.08$ at 15 arcsec resolution. The fact that the spectral index is consistent in this region at both resolutions suggests that this steepening is physical. Again, we do not currently have the signal to noise to investigate this further; deeper low-frequency observations would be required to study the spectral index behaviour in the cluster outskirts in more detail and confirm this steepening.

Due to the sensitivity difference between our MeerKAT and LOFAR images, the outermost regions of the mini-halo are undetected at 145 MHz; however, given that they are undetected by LOFAR they cannot have an ultra-steep spectrum. To quantify the spectral index limit in the outer reaches of the mini-halo, we take the typical surface brightness measured by MeerKAT and assume a 2.5σ limit from our LOFAR map. This yields an upper limit to the spectral index of $\alpha \gtrsim -1.3$. Deeper observations with LOFAR would be required to map the spectral index in these regions; however, the spectral index in these outer regions is clearly shallower than the ultra-steep values of $\alpha \sim -2$ to -3 measured by Biava et al. (2021) in the outer regions of RX J1720.1+2638.

4.2 Surface brightness profiles

4.2.1 Radio surface brightness

Given the asymmetric nature of the mini-halo in MS 1455.0+2232, we might expect to detect the presence of multiple radio components. Such multicomponent nature has only been found in a handful of mini-haloes to date (Savini et al. 2018, 2019; Biava et al. 2021). Our observations provide the first hints of radio substructure in this cluster.

We investigated the radial surface brightness profiles of both our radio and X-ray data in our high-resolution (8 arcsec) source-subtracted images. We used two 'wedges' centred on the BCG, each covering a 50 deg arc – a 'north wedge' pointing towards the north of MS 1455.0+2232 (where the radio contours are tightly packed) and a 'south wedge' directed to the south-west where the radio contours are less tightly packed. Panels (a) and (b) of Fig. 10 show the wedge regions overlaid atop our MeerKAT 1283 MHz / LOFAR 145 MHz and *Chandra* data.

Panels (c), (d), and (e) of Fig. 10 show the azimuthally averaged surface brightness profile for each wedge. At both frequencies, the

Downloaded from https://academic.oup.com/mnras/article/512/3/4210/6547010 by guest on 07 March 2025

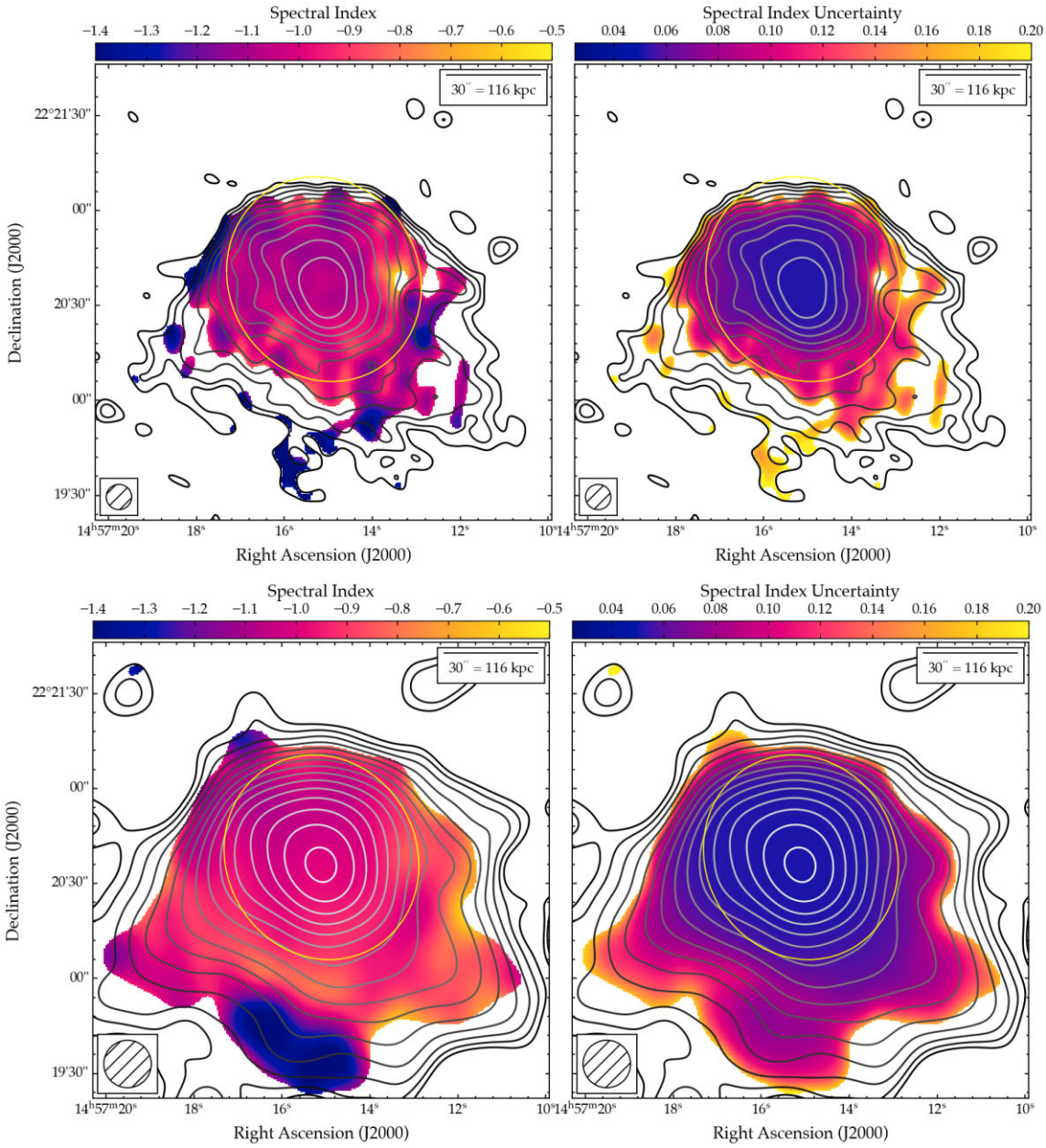


Figure 9. Spectral index map (*left*) and associated uncertainty (*right*) of the mini-halo in MS 1455.0+2232 at a resolution of 8 arcsec (*top*) and 15 arcsec (*bottom*), derived using our MeerKAT (1283 MHz) and LOFAR (145 MHz) data. Contours show MeerKAT surface brightness at 1283 MHz as per Fig. 3. Pixels below 3σ in each radio image are blanked. The yellow ellipse traces the outer boundary of the sloshing spiral, as per Fig. 5.

radio surface brightness profile of each wedge appears to follow a roughly exponential decrease with increasing radius out to about ∼100 kpc. However, beyond a distance of around 100 kpc, the behaviour of the radio surface brightness diverges significantly. For the north wedge, the surface brightness decreases sharply; conversely, for the south wedge, a second component emerges. This component also appears to follow a broadly exponentially decreasing surface brightness profile, and is common to both our MeerKAT and LOFAR data. This provides clear evidence that MS 1455.0+2232 hosts a multicomponent radio mini-halo.

Typically, a standard circular exponential profile is used to model the surface brightness of haloes and mini-haloes (e.g. Cassano et al. 2007; Murgia et al. 2009; Bonafede et al. 2017). This profile takes the form:

$$I_{\rm R}(r) = I_{\rm R,c} \exp\left(-r/r_e\right) , \tag{3}$$

where $I_{\rm R,c}$ is the central radio surface brightness and r_e is the e-folding radius, typically found to be $\sim R_{\rm H}/2.6$ for a radio halo of radius $R_{\rm H}$ (e.g. Bonafede et al. 2017). However, given the multicomponent nature of the diffuse radio emission seen in the south wedge, we can infer that this component likely also underlies the profile seen in the north wedge. In any case, a single exponential does not provide a good description of the radio surface brightness of the mini-halo in MS 1455.0+2232.

Recently, Boxelaar, van Weeren & Botteon (2021) have presented a novel algorithm (the Halo Flux Density Calculator, or HALO-FDCA)

Downloaded from https://academic.oup.com/mnras/article/512/3/4210/6547010 by guest on 07 March 2025

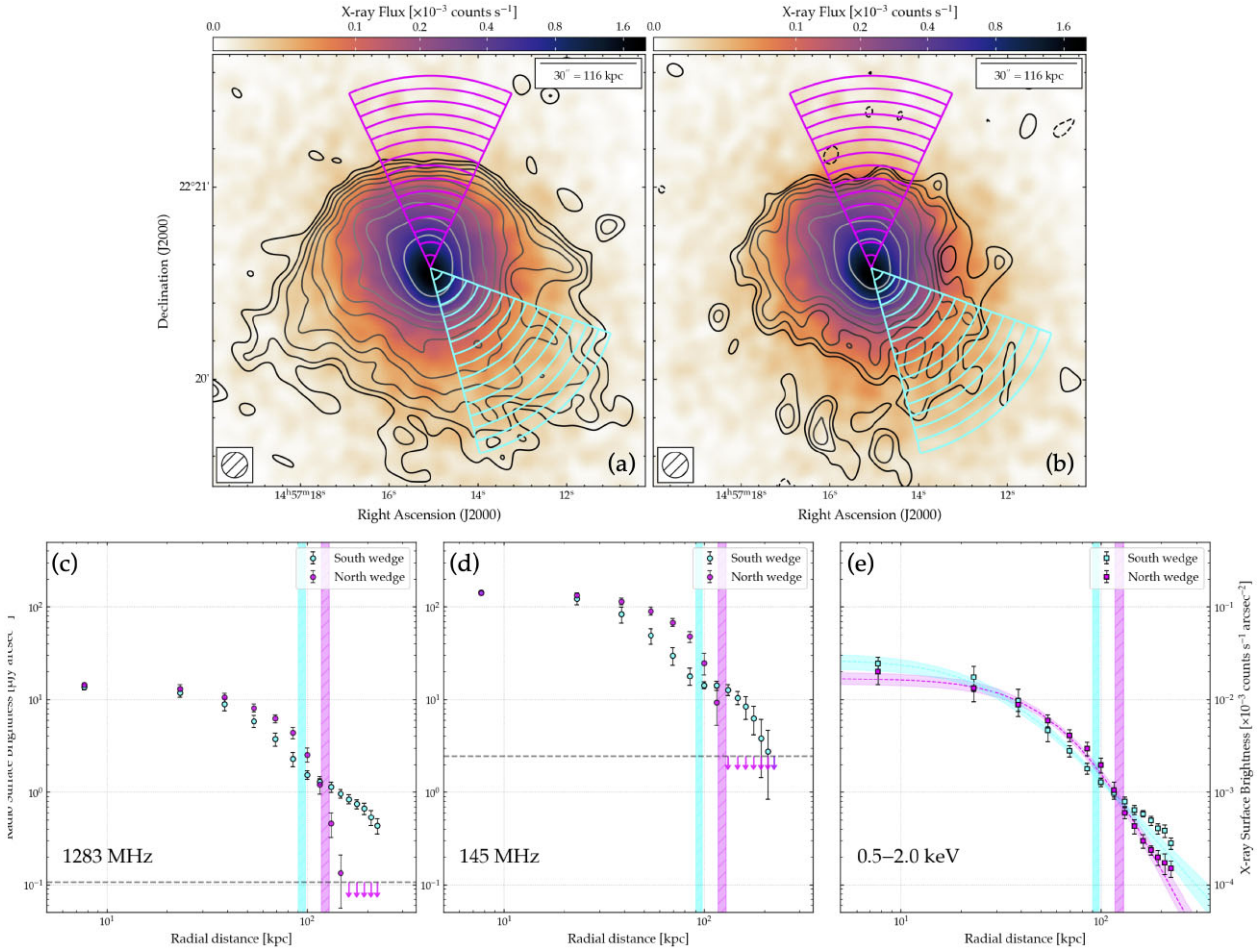


Figure 10. *Upper:* radio/X-ray overlays of the mini-halo in MS 1455.0+2232. Colourmap in each panel shows our source-subtracted *Chandra* data, smoothed with a Gaussian of FWHM 8 arcsec. Contours show our source-subtracted radio data at 8 arcsec resolution, with MeerKAT 1283 MHz in panel (a) and LOFAR 145 MHz in panel (b). These contours start at 3σ and scale by a factor $\sqrt{2}$. The 'north wedge' (magenta) and 'south wedge' (cyan) extraction regions used to model the radial profiles are also overlaid. *Lower:* azimuthally averaged radial profiles for the 'north wedge' and 'south wedge' extracted from our multiwavelength data, colourized as per panels (a) and (b). Panels (c), (d), and (e) respectively show the profiles extracted from our MeerKAT (1283 MHz), LOFAR (145 MHz), and *Chandra* (0.5–2.0 keV) data. Curves in panel (e) denote the best-fitting beta model and 1σ uncertainty. The horizontal dashed line indicates the 1σ level in the respective radio map. Vertical shaded regions mark the outer edge of the sloshing spiral, as measured along each arc (see Fig. 4).

for the measurement of the total flux density from diffuse haloes in galaxy clusters. While this algorithm employs a full MCMC treatment, all models currently implemented by HALO-FDCA rely on the radio surface brightness profile following a single exponential profile.[6] As demonstrated here however, the surface brightness profile of the mini-halo in MS 1455.0+2232 cannot be described by a single exponential.

4.2.2 X-ray surface brightness

The X-ray surface brightness profile recovered by *Chandra* is strikingly different however. It is not immediately obvious whether there is evidence of substructure, as the radial profiles show a similar surface brightness decrease as a function of radius. We attempt to model the behaviour using a standard beta-model, which follows the assumption of an isothermal gas profile and spherical geometry (see e.g. Cavaliere & Fusco-Femiano 1976, 1978; Ettori 2000). This beta model takes the form:

$$I_{\rm X}(r) = I_{\rm X,c}\left(1+\left(\frac{r}{r_{\rm c}}\right)^2\right)^{(0.5-3\beta)}, \quad (4)$$

where $r_{\rm c}$ is the core radius and $I_{\rm X,\,c}$ is the central X-ray surface brightness. As with the BCG SED, we used EMCEE to constrain the parameters of equation (4). These fits are also presented in Fig. 10.

While the X-ray surface brightness profile of the north wedge is reasonably well-described by a single beta-model, the profile of the south wedge shows an X-ray surface brightness excess beyond around 150 kpc radius. Additionally, we find that the two profiles are not described by the same values of $r_{\rm c}$ or β: for the north wedge, we find $r_{\rm c,\,n} = 72.6 \pm 9.2$ kpc and $\beta_{\rm n} = 0.91 \pm 0.08$, whereas for the south wedge we find $r_{\rm c,\,s} = 30.9 \pm 7.2$ kpc and $\beta_{\rm s} = 0.58 \pm 0.06$. This provides further evidence of substructure in the ICM of MS 1455.0+2232, and is in agreement with the extension of the diffuse X-ray surface brightness seen in Fig. 4.

Overall, our evidence indicates that the mini-halo in MS 1455.0+2232 shows remarkably different behaviour in az-

[6]Whether circular, elliptical, or skewed – see https://github.com/JortBox/Halo-FDCA.

Downloaded from https://academic.oup.com/mnras/article/512/3/4210/6547010 by guest on 07 March 2025

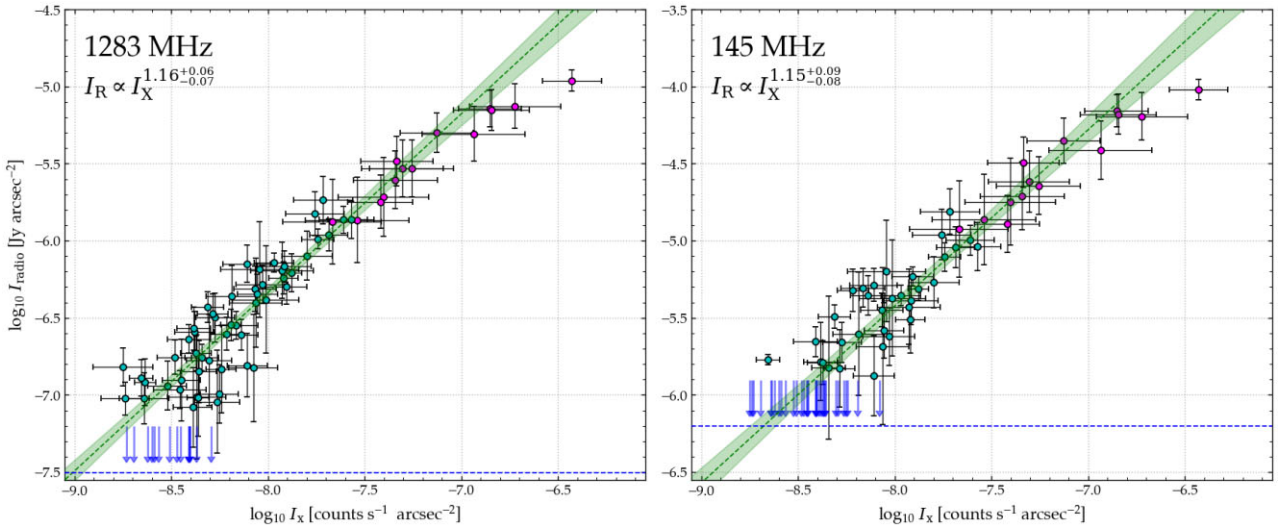


Figure 11. Radio/X-ray surface brightness correlation for the mini-halo in MS 1455.0+2232. *Left-hand panel* shows the I_R/I_X plane at 1283 MHz, measured from our MeerKAT image, *right-hand panel* shows the same plane at 145 MHz measured from our LOFAR image, both at 15 arcsec resolution. Data-point markers are colourized according to the extraction region (seen in Fig. 5). Magenta data points lie within the bounds of the sloshing spiral; cyan data points lie outside the sloshing spiral boundary. For regions where the radio surface brightness is below the 3σ level in the corresponding image, we adopt a 2σ upper limit in this analysis; these are indicated by blue arrows, and the dashed blue line indicates the 1σ level. Dashed green line shows the best-fitting power-law relation derived using LINMIX, and the shaded green region shows the 1σ uncertainty. The slope of the best-fitting power-law is $b_{1283\,\mathrm{MHz}} = 1.16^{+0.06}_{-0.07}$ at 1283 MHz and $b_{145\,\mathrm{MHz}} = 1.15^{+0.09}_{-0.08}$ at 145 MHz.

imuthally averaged radial surface brightness between radio and X-ray wavelengths. To the best of our knowledge, there are no other sufficiently well-resolved mini-haloes where the radial profile has been studied in similar detail. However, we note that this behaviour is in contrast with what has typically been seen for radio haloes, which show a generally similar radial profile at both radio and X-ray wavelengths (e.g. Hoang et al. 2021; Rajpurohit et al. 2021b).

4.3 Thermal/non-thermal comparison

4.3.1 Point-to-point correlation: surface brightness

In radio haloes, the synchrotron emission often shows a similar morphology and extent to the observed X-ray emission (van Weeren et al. 2019, and references therein). Mini-haloes show a similar trend, albeit covering a smaller fraction of the cluster volume, although that may be due to the relatively limited sensitivity of many historic observations (for example Giacintucci et al. 2019; Ignesti et al. 2020; Biava et al. 2021). This implies a connection between the thermal and non-thermal components in the ICM. Fig. 5 shows the *Chandra* X-ray image of MS 1455.0+2232 in the $0.5 - 2.0$ keV band, smoothed to a resolution of 15 arcsec, with source-subtracted radio contours overlaid. As can be seen in Fig. 5, the mini-halo in MS 1455.0+2232 fills the entire volume of the X-ray emitting region, indicating a strong connection.

We studied the radio/X-ray connection using the point-to-point correlation between the radio surface brightness (I_R) and X-ray surface brightness (I_X) at 15 arcsec resolution. Following recent similar studies (such as Botteon et al. 2020a; Ignesti et al. 2020; Biava et al. 2021; Duchesne, Johnston-Hollitt & Wilber 2021a; Rajpurohit et al. 2021a, b, although most of these have focused on giant haloes), we place adjacent boxes of 15 arcsec width across the mini-halo in MS 1455.0+2232, covering all regions above an X-ray flux limit of $\sim 5 \times 10^{-7}$ counts s^{-1}, excising those regions contaminated by residual emission from radio galaxies. These boxes are also shown in Fig. 5.

The I_R/I_X plane for the MS 1455.0+2232 mini-halo is presented in Fig. 11. Our new highly sensitive radio data show a positive correlation between radio and X-ray surface brightness, suggesting a strong connection between the thermal and non-thermal components in the mini-halo hosted by MS 1455.0+2232. To quantify the connection, we fit a power-law relation (in log-log space) of the form:

$$\log(I_R) = c + b\log(I_X), \tag{5}$$

where the slope b describes the scaling between the thermal and non-thermal components of the ICM. The slope of this correlation is related to the underlying particle acceleration mechanism (e.g. Govoni et al. 2001; Brunetti et al. 2004; ZuHone et al. 2013, 2015). Broadly speaking, the turbulent (re-)acceleration scenario can produce either a sub-linear or super-linear slope depending on the nature and distribution of the relativistic electrons throughout the cluster volume. Generally, the hadronic model predicts a super-linear relation due to the central CRp injection profile and equipartition assumption.

Physically, the slope relates to the relative distribution of non-thermal and thermal components. A super-linear slope (i.e. $b > 1$) would indicate that the magnetic field and/or CRe distribution is more peaked than the thermal plasma distribution, whereas a sub-linear slope (i.e. $b < 1$) would indicate the converse. However, different magnetic field profiles and/or CRp density profiles (which might arise due to the relative contribution from cluster-member galaxies) can yield different correlation slopes (e.g. Ignesti et al. 2020; Timmerman et al. 2021).

In the sample of seven mini-haloes studied by Ignesti et al. (2020) with archival GMRT and VLA observations, the point-to-point analysis revealed a consistently super-linear slope in the I_R/I_X plane. However, due to the limited surface-brightness sensitivity and resolution of the available data, the slope of the point-to-point

Downloaded from https://academic.oup.com/mnras/article/512/3/4210/6547010 by guest on 07 March 2025

Table 3. Summary of results for our LINMIX fitting routines, fitting the point-to-point correlation between X-ray surface brightness and either the radio surface brightness at the listed frequency or spectral index, as indicated in the first column. b is the best-fitting correlation slope for the plane, and r_S and r_P are respectively the Spearman and Pearson correlation coefficient for each plane. The fit for the spectral index point-to-point analysis was performed using only measurements outside the sloshing spiral (cyan data points in Fig. 12).

Image	Slope b	Spearman coeff. r_S	Pearson coeff. r_P
1283 MHz	$1.16^{+0.06}_{-0.07}$	0.91	0.94
145 MHz	$1.15^{+0.09}_{-0.08}$	0.89	0.95
α (outer)	$0.21^{+0.11}_{-0.11}$	0.28	0.28

correlations presented by Ignesti et al. often show significant scatter and thus significant uncertainty.

We determined the best-fitting values of a and b, and quantified the strength of our correlation, using the LINMIX software package[7] (Kelly 2007). LINMIX performs Bayesian linear regression, accounting for uncertainties on both variables, intrinsic scatter, and (importantly) upper limits to the dependent variable (I_R). We used the MCMC implementation incorporated in LINMIX to determine the best-fitting values for a and b. We quote the median values of a and b from our MCMC run as our 'best-fitting' values, and use the 16th and 84th percentiles to determine the uncertainties. Finally, the correlation strength was quantified by measuring the Spearman and Pearson rank coefficients.

Table 3 presents the results of our fitting routine. We measure a slope of $b_{145\,\mathrm{MHz}} = 1.15^{+0.09}_{-0.08}$ for the LOFAR/*Chandra* surface brightness plane and $b_{1283\,\mathrm{MHz}} = 1.16^{+0.06}_{-0.07}$ for the MeerKAT/*Chandra* surface brightness plane. We find that the radio and X-ray surface brightness is well-correlated at each frequency, with a Pearson (Spearman) coefficients of $r_p = 0.89$ ($r_s = 0.95$) at 145 MHz and $r_p = 0.91$ ($r_s = 0.94$) at 1283 MHz. At each frequency, the slope is super-linear, consistent with the typical behaviour of mini-haloes in the I_R/I_X plane (e.g. Govoni et al. 2009; Ignesti et al. 2020; Biava et al. 2021). This super-linear correlation is generally believed to favour the hadronic model over the turbulent re-acceleration scenario, although we note that under some conditions, the turbulent (re-)acceleration model can replicate a super-linear slope. These conditions include scenarios where turbulence is stronger in the central region and/or where the spatial distribution of CRe is more peaked towards the cluster centre than the thermal electron distribution (see simulations by ZuHone et al. 2013, for example).

The mini-halo sample of Ignesti et al. (2020) includes MS 1455.0+2232. The analyses are not straightforward to compare due to the dramatic difference in surface brightness sensitivity achieved by our MeerKAT and LOFAR images compared to the narrow-band GMRT images used by Ignesti et al. (2020). Similarly, the methods employed differ somewhat. Ignesti et al. (2020) use two different methods to study the point-to-point correlation, the results of which exhibit a mild tension: the BCES Bisector method finds a best-fitting slope $k = 0.83 \pm 0.10$, whereas they derive a correlation slope of $k = 1.00 \pm 0.12$ from the subsequent Monte Carlo analysis using the Point-to-point TRend EXtractor (PT-REX; Ignesti 2022). In either case, our LINMIX regression yields a fit that is steeper than that found by Ignesti et al. (2020).

[7]LINMIX is available through https://linmix.readthedocs.io/en/latest/src/linmix.html

Our new broad-band data not only allow us to study the point-to-point comparison in exquisite detail, but also to investigate whether there is any evolution in the correlation with frequency. Two of the seven mini-haloes in the sample of Ignesti et al. (2020) have multifrequency data available at 610 MHz and 1.4 GHz. While both show super-linear slopes at each frequency, one (Abell 3444) shows no change in the correlation slope moving to higher frequency, whereas the other (2A 0335+096) shows a slight flattening of the correlation slope with increasing frequency. Recently, LOFAR observations of 2A 0335+096 revealed that the correlation slope also shows super-linear scaling at 144 MHz (albeit with large uncertainties, due to the presence of several sub-structures embedded in the mini-halo; for further details see Ignesti et al. 2022).

For radio haloes, few studies have the necessarily high-resolution multifrequency radio data required to investigate this. However, from these few studies, the picture is also mixed: the radio haloes in Abell 520 and Abell 2744 show no change in the correlation slope with frequency (respectively Hoang et al. 2019; Rajpurohit et al. 2021b), whereas the radio haloes hosted by ClG 0217+70, MACS J0717.5+3745, and Abell 2256 do exhibit a change in correlation slope with frequency (respectively Hoang et al. 2021; Rajpurohit et al. 2021a, Rajpurohit et al. in preparation). For MACS J0717.5+3745 and Abell 2256, the correlation slope steepens toward higher frequencies, which implies spectral index steepening, in line with the turbulent (re-)acceleration scenario under certain physical conditions. Conversely, ClG 0217+70 exhibits a flatter correlation slope toward higher frequency, suggesting that further non-thermal processes play a role in the cluster outskirts where the X-ray emission is fainter. See the discussion in the aforementioned papers for further details.

Our analysis indicates no significant evolution in the slope with frequency – the slope of the correlation is consistent at 1283 and 145 MHz. However, the comparison between our MeerKAT and LOFAR images shows that we cannot yet map the full extent of the mini-halo at 145 MHz; deeper observations with LOFAR, and/or follow-up observations at complementary frequencies would be required to investigate this further. This implies that we are not seeing any evidence of spectral steepening, consistent with evidence presented earlier, although we again note that higher-frequency observations (e.g. at S- or C-band) would be required to investigate further.

4.3.2 *Point-to-point correlation: spectral index*

Our highly-sensitive data also allow us to study the point-to-point relation between the radio spectral index and the X-ray surface brightness. We also performed this analysis using our images at 15 arcsec resolution. Few such studies exist in the literature for mini-haloes, though Biava et al. (2021) found no strong correlation between spectral index and X-ray surface brightness for the mini-halo in RX J1720.1+2638. Outside of the mini-halo however, Biava et al. (2021) find a moderate-to-strong anticorrelations for the different diffuse radio emission substructures outside the core of RX J1720.1+2638.

For radio haloes, the picture is mixed. Some haloes show positive correlation (Botteon et al. 2020b), some show an anticorrelation (Rajpurohit et al. 2021a) and others show both correlation and anticorrelation for different sub-regions (Rajpurohit et al. 2021b). We quantified the relation between radio spectral index α and X-ray surface brightness in by fitting a power law in linear-log space as

Downloaded from https://academic.oup.com/mnras/article/512/3/4210/6547010 by guest on 07 March 2025

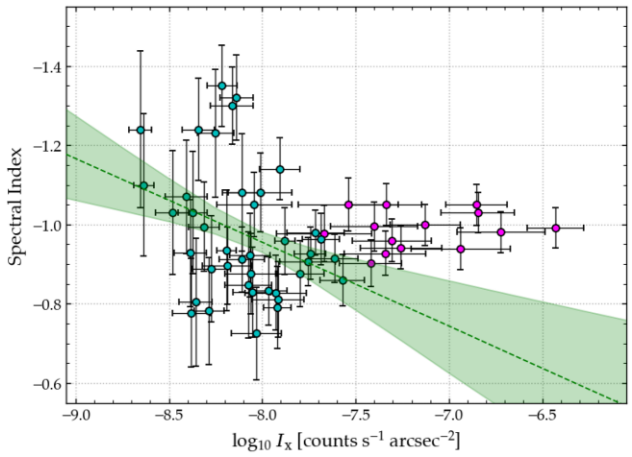


Figure 12. Radio spectral index/X-ray surface brightness correlation for the mini-halo in MS 1455.0+2232. Data points are colourized according to extraction region, as per Fig. 5. Magenta points denote regions inside the boundary of the sloshing spiral, cyan points denote regions exterior to the sloshing spiral. Note the inverted y-axis to facilitate comparison with previous similar studies. Dashed green line shows the best fit to equation (6) for the cyan data points, derived using LINMIX, and the shaded green region shows the 1σ uncertainty. The slope is $b = 0.21 \pm 0.11$. Magenta points show no correlation.

follows:

$$\alpha = c + b\log(I_{\rm X}) \tag{6}$$

The result of our point-to-point analysis is presented in Fig. 12, and the correlation slope b and Spearman and Pearson coefficients are reported in Table 3. When we fit a single relation to all data points, the slope $b = 0.01^{+0.03}_{-0.03}$ is consistent with no correlation. The Spearman and Pearson coefficients are similarly very weak, as we find $r_{\rm S} = 0.07$ and $r_{\rm P} = -0.01$. However, Fig. 12 suggests that regions inside and outside the sloshing spiral may exhibit different behaviour: regions outside the sloshing spiral (cyan points in Fig. 12) appear to show a tentative correlation with X-ray surface brightness, similar to the 'eastern extension' of the mini-halo in RX J1720.1+2638 (Biava et al. 2021). While the correlation is weak ($r_{\rm S} = 0.28$ and $r_{\rm P} = 0.28$), we find a best-fitting slope $b = 0.21^{+0.11}_{-0.11}$. This fit is presented in Fig. 12. The magenta points show no correlation.

Fig. 12 also demonstrates that the standard deviation in spectral index increases in the fainter X-ray regions outside the sloshing spiral, as mentioned previously in Section 4.1.3. Overall, this evidence supports the multicomponent mini-halo interpretation, though the limited sensitivity of our LOFAR data prevents us from exploring this in more detail at present.

5 DISCUSSION

One of the key unanswered questions in the study of mini-haloes is the underlying acceleration mechanism. In previous sections, we have presented the evidence from our multiwavelength analysis and examined each piece in isolation. In this section, we will draw all our evidence together and attempt to determine whether the mini-halo in MS 1455.0+2232 is consistent with the hadronic scenario or the turbulent (re-)acceleration scenario.

5.1 Key observables

In order to try and differentiate between the underlying acceleration mechanisms, we must examine which scenario 'best' reproduces the findings of our analysis. We summarize the key findings below:

(i) The presence of a relatively asymmetric and highly extended mini-halo ∼590 kpc in extent.
(ii) An average spectral index of $\alpha \simeq -1$ that is largely consistent over much of the synchrotron-emitting volume. Spectral index fluctuations are seen toward larger radii, although no overall steepening trend is evident (aside from a select region to the south).
(iii) The presence of multiple radio components seen in the azimuthally averaged radial surface brightness profiles to the south of the cluster, but *not* the north.
(iv) The existence of a large-scale sloshing spiral (visible in both the X-ray gradient and entropy maps) which does not bound the detected synchrotron emission.
(v) A super-linear scaling relation between X-ray surface brightness and radio surface brightness at both measured frequencies, with a power-law index $b \simeq 1.15$.

In both the turbulent (re-)acceleration scenario and the hadronic scenario, the radio emission production density $\dot{\varepsilon}_{\rm R}$ scales approximately with the product of the magnetic field energy densities (ε_B) and CRe energy density ($\varepsilon_{\rm CRe}$), respectively, as:

$$\dot{\varepsilon}_{\rm R} \propto \varepsilon_B \cdot \varepsilon_{\rm CRe} \tag{7}$$

The X-ray emission production density ($\dot{\varepsilon}_{\rm X}$) depends on the electron density ($n_{\rm e}$), gas temperature ($T_{\rm e}$), and thermal gas energy density ($\varepsilon_{\rm th} \propto n_{\rm e}\, T_{\rm e}$) following:

$$\dot{\varepsilon}_{\rm X} \propto n_{\rm e}^2 \cdot T_{\rm e}^{0.5} \propto \varepsilon_{\rm th}^2 \cdot T_{\rm e}^{-1.5} \tag{8}$$

Thus, the relation between radio and X-ray emissivities is tied to the dependence of ε_B and $\varepsilon_{\rm CRe}$ on $n_{\rm e}$, $\varepsilon_{\rm th}$, and $T_{\rm e}$. This relation differs between the two scenarios.

5.2 Turbulent (re-)acceleration scenario

In this scenario, the CRe are powered by turbulent (re-)acceleration of electrons in the ICM by sloshing motions within the cool core. Our *Chandra* analysis has revealed that MS 1455.0+2232 is experiencing large-scale core sloshing on scales up to ∼1.1 arcmin (∼254 kpc) in extent; as such, turbulence likely plays a role in powering the mini-halo. The presence of breaks in the radio surface brightness profiles corresponding to the outer boundaries of the sloshing spiral indicates that there must be a strong connection between the dynamics of the thermal gas and the non-thermal components within this region.

Turbulence is inherently an intermittent process, both spatially and temporally. Spatial intermittence implies that the observed radio spectrum, along a given line of sight, can result from the superposition of different components with different spectral properties. Temporal intermittence implies that the classical steady-state spectra are not necessarily achieved by the CRe distribution at different locations. As such, in the turbulent (re-)acceleration scenario, we might expect to see spatial variations in the radio emission (at a given frequency) and thus fluctuations in the spectral index distribution.

Our analysis shows that at 15 arcsec resolution, the spectral index is broadly uniform across much of the mini-halo volume. When viewed at 8 arcsec resolution, we see more significant fluctuation. In principle, the absence of strong spectral variations may be reconciled with (re-)acceleration assuming that different turbulent cells are integrated along the line of sight; the appearance of spectral

Downloaded from https://academic.oup.com/mnras/article/512/3/4210/6547010 by guest on 07 March 2025

variations at higher resolution might be suggestive of this possibility. Furthermore, the average spectral index profile is slightly steeper (and exhibits greater standard deviation) outside the sloshing spiral boundary than within the spiral. This may arise naturally in a scenario where the turbulence is injected by the large-scale sloshing spiral visible in MS 1455.0+2232.

However, the mini-halo extends far beyond the boundaries of the sloshing spiral, and while the X-ray surface brightness shows evidence of a low-level excess following the 'tail' of emission to the south/south-west of the mini-halo, we find no significant evidence of any large-scale sloshing in this region. The scaling between radio and X-ray surface brightness is less predictive in this scenario. It depends on the fine details of the turbulence mechanism and how turbulence causes particle acceleration and magnetic field amplification. Simulations of turbulent (re-)acceleration in sloshing cores can yield a super-linear scaling relation (ZuHone et al. 2013), although the extent to which this conclusion depends on the fine-tuning of simulation parameters (dynamical parameters and the turbulent acceleration model) is not explored in the literature.

5.3 Hadronic scenario

In the hadronic scenario, the CRe are produced by inelastic collisions between CRp and thermal protons in the ICM. Thus, the CRp spectrum imprints on to the observed spectrum of the CRe, as:

$$\dot{\varepsilon}_{\rm CRe} \propto n_{\rm e} \cdot \varepsilon_{\rm CRp}, \tag{9}$$

where $\varepsilon_{\rm CRp}$ is the CRp energy density. In galaxy cluster environments, CRp are long-lived and are thus in principle able to achieve a spatially smooth distribution that exhibits a similar spectral slope throughout the volume of the cluster. As such, the largely smooth spectral index we observe for this mini-halo is naturally explained by the hadronic scenario.

The CRe generated by the inelastic collisions are short lived, due to their radiative losses via synchrotron and inverse Compton emission, and therefore should quickly establish a steady-state electron energy density according to:

$$\varepsilon_{\rm CRe} = \dot{\varepsilon}_{\rm CRe} \cdot \tau_{\rm loss} \propto \frac{n_{\rm e} \cdot \varepsilon_{\rm CRp}}{\varepsilon_B + \varepsilon_{\rm CMB}}, \tag{10}$$

where $\varepsilon_{\rm CMB}$ is the CMB energy density and $\tau_{\rm loss}$ is the time-scale over which the electrons radiate their energy. Thus, in the hadronic model we expect a relation of the radio emissivity to the basic plasma parameters as:

$$\begin{aligned}\dot{\varepsilon}_{\rm R} &\propto \frac{\varepsilon_B}{\varepsilon_B + \varepsilon_{\rm CMB}} \cdot \varepsilon_{\rm CRp} \cdot n_{\rm th} \\ &\propto (1 + \varepsilon_{\rm CMB}/\varepsilon_B)^{-1} \cdot \varepsilon_{\rm CRp} \cdot \varepsilon_{\rm th} \cdot T_{\rm e}^{-1}.\end{aligned} \tag{11}$$

As such, by comparing equations (8) and (11), we find that we would achieve a linear scaling between X-ray and radio emission if three conditions are fulfilled:

(i) The energy density of CRp and thermal protons are proportional ($\varepsilon_{\rm CRp} \propto \varepsilon_{\rm th}$).
(ii) The core is isothermal ($T_{\rm e} = $ const.).
(iii) The magnetic field energy density is much greater than the energy density of the CMB ($\varepsilon_B \gg \varepsilon_{\rm CMB}$, i.e. $B \gg 5$ μG).

In case of weaker magnetic fields, with energy densities $\varepsilon_B \ll \varepsilon_{\rm CMB}$ roughly scaling with the thermal energy density ($\varepsilon_B \propto \varepsilon_{\rm th}$), we would find a strong super-linear scaling relation. In this case, $\dot{\varepsilon}_{\rm R}/\dot{\varepsilon}_{\rm X} \propto \varepsilon_{\rm th} \cdot T_{\rm e}^{0.5}$. As such, assuming a magnetic field in the cluster core of $B \sim B_{\rm IC}$, the observed slightly super-linear scaling relation between radio and X-ray surface brightness arises as a natural consequence of the hadronic model. However, a full investigation of the specific details of the hadronic scenario that are constrained by our observations (similar to, e.g. Enßlin et al. 2011; Ignesti et al. 2020) is beyond the scope of this paper.

Another important piece of evidence comes from the precipitous drop of the radio brightness observed across the boundary of the sloshing spiral in the north wedge region in Fig. 10. In a purely hadronic scenario, this would require a significant drop of the magnetic field across this boundary, provided that CRp are distributed on large scales in the ICM and that $B \sim B_{\rm IC} \simeq 4 - 10$ μG. Simulations of the hadronic scenario by ZuHone et al. (2015) do predict a drop in B across the sloshing boundary by a factor 5 or 6; however, in order to explain our observations, a much larger decrease of a factor of at least 30–70 in the magnetic field energy density is required (G. Brunetti, private commnication).

One means by which we can reconcile the hadronic scenario with our observations is to assume that most of the CRp were generated by the central BCG and are confined by the large-scale magnetic field. Thus, the diffusion time-scale required is $\tau \sim 5/D_{30}$ Gyr, where D_{30} is the spatial diffusion coefficient in units of 10^{30} cm^2 s^{-1} (Brunetti & Jones 2014). As with the turbulent (re-)acceleration scenario, detailed modelling is beyond the scope of this paper.

The evidence provided by our *Chandra* data also cannot be ignored. The large-scale sloshing does not arise in a purely hadronic scenario. Similarly, we observe both a steepening of the spectral index, as well as an increase in standard deviation for regions outside the boundary of the sloshing spiral compared to those regions in the interior. This implies a connection with the large-scale motions within the ICM that is not anticipated in a purely hadronic scenario.

5.4 Overall picture

Based on the arguments laid out in this section, both the turbulent (re-)acceleration scenario and the hadronic scenario are naturally able to explain many of the observables. However, neither scenario is satisfactorily able to explain all pieces of evidence provided by our detailed multiwavelength analysis. As such, we are unable to conclusively determine whether one scenario is preferred, or whether a hybrid scenario – some combination of hadronic emission plus turbulent acceleration, perhaps dominant on different scales (e.g. Brunetti & Lazarian 2011; Zandanel, Pfrommer & Prada 2014) – provides the best explanation. We will return to this in future with the full sample from our MeerKAT-meets-LOFAR mini-halo census, in conjunction with deeper theoretical exploration of the scenarios.

6 CONCLUSIONS

In this paper, we have presented the first highly sensitive multifrequency study of the mini-halo hosted by the cluster MS 1455.0+2232, using data from the MeerKAT and LOFAR radio telescopes at 1283 and 145 MHz, respectively. These data, combined with archival X-ray data from *Chandra*, have allowed us to perform a comprehensive and detailed study of the connection between the thermal and non-thermal properties of the mini-halo.

We find that the mini-halo fills the overwhelming majority of the X-ray emitting region traced by *Chandra*, suggesting a strong connection between the thermal and non-thermal properties of the ICM. From our MeerKAT image at 1283 MHz, the LLS of this 'mini'-halo is 586 kpc, 69 per cent larger than was previously reported, emphasizing the need for highly sensitive radio observations of these

Downloaded from https://academic.oup.com/mnras/article/512/3/4210/6547010 by guest on 07 March 2025

relaxed clusters when attempting to understand the thermal/non-thermal connection.

Our re-analysis of deep *Chandra* observations have revealed striking evidence of a large-scale asymmetric sloshing spiral in MS 1455.0+2232, identified in the X-ray gradient map. The lower-entropy regions of the ICM follow the structure traced by the sloshing spiral.

We measure a total integrated flux density of $S_{1283\,\mathrm{MHz}} = 18.7 \pm 0.9$ mJy and $S_{145\,\mathrm{MHz}} = 154.5 \pm 15.6$ mJy for the diffuse emission from the mini-halo. The mini-halo has an integrated spectral index $\alpha^{145\,\mathrm{MHz}}_{1283\,\mathrm{MHz}} = -0.97 \pm 0.05$. The 2D spectral index map is broadly uniform at 15 arcsec resolution, although it exhibits more significant fluctuations at 8 arcsec resolution, perhaps suggesting the blurring of different substructures by the larger PSF. We find tentative evidence that the average spectral index is marginally steeper outside the boundary of the sloshing spiral; the spectral index exhibits a factor $\sim$1.5–2 greater standard deviation outside the boundary.

We have profiled the behaviour of the radio and X-ray surface brightness, as measured along two arc-shaped wedges from the BCG out to large radius. The radio surface brightness follows a roughly exponential drop-off (although it is poorly described by standard radio halo profiles) out to the boundaries of the sloshing spiral. Outside the spiral boundary to the north, the radio surface brightness decreases precipitously; to the south, however, we find significant evidence of additional diffuse radio emission indicating the presence of substructure. At present though, we are unable to explore it further.

We have studied the spatial correlation between X-ray surface brightness and (i) radio surface brightness and (ii) radio spectral index. Our analysis reveals a tight correlation in the $I_\mathrm{R}/I_\mathrm{X}$ plane with a conclusively super-linear slope at both 1283 and 145 MHz. We find the slope of correlation (i) to be $b_{1283\,\mathrm{MHz}} = 1.16^{+0.06}_{-0.07}$ at 1283 MHz and $b_{145\,\mathrm{MHz}} = 1.15^{+0.09}_{-0.08}$ at 145 MHz. For correlation (ii), we find that regions inside the sloshing spiral exhibit no correlation, whereas regions outside the spiral show a relatively weak correlation with a slope $b = 0.21 \pm 0.11$. This provides further evidence in favour of substructure.

Additionally, we have used our new MeerKAT and LOFAR data in conjunction with historic narrow-band radio observations to explore the broad-band radio SED of the BCG in MS 1455.0+2232. The spectral index exhibits a clear break, and is well-described by a broken power law with a flat low-frequency spectral index $\alpha_\mathrm{low} = -0.45 \pm 0.05$ and a typical synchrotron spectral index $\alpha_\mathrm{high} = -0.81 \pm 0.18$ above the break. Due to the relatively sparse sampling of the ancillary data involved however, the break frequency remains relatively poorly constrained, as we find $\nu_\mathrm{b} = 3.1 \pm 1.4$ GHz.

Finally, we have attempted to determine whether the hadronic model or the turbulent (re-)acceleration scenario is best able to explain all the evidence provided by our observations. While both scenarios are able to explain some observables, neither is satisfactorily able to explain all the evidence. As such, this paper may serve to spark new theoretical work examining the detailed physics of particle acceleration mechanisms in sloshing cool-core clusters. MS 1455.0+2232 represents the first of 13 mini-haloes which our team is studying in detail using deep MeerKAT and LOFAR data; the remainder of our mini-halo census promises to provide a revolutionary step in our understanding of mini-halo physics.

ACKNOWLEDGEMENTS

CJR, NB, AB, EB, and CS acknowledge financial support from the ERC Starting Grant 'DRANOEL', number 714245. KR acknowledges financial support from the ERC Starting Grant 'MAGCOW', number 714196. AB acknowledges support from the VIDI research programme with project number 639.042.729, which is financed by the Netherlands Organisation for Scientific Research (NWO). FL acknowledges financial support from the Italian Minister for Research and Education (MIUR), project FARE, project code R16PR59747, project name FORNAX-B. FL acknowledges financial support from the Italian Ministry of University and Research – Project Proposal CIR01_00010. RT and RJvW acknowledge support from the ERC Starting Grant ClusterWeb 804208. GDG acknowledges support from the Alexander von Humboldt Foundation. AI acknowledges the Italian PRIN-Miur 2017 (PI A. Cimatti). CS acknowledges support from the MIUR grant FARE 'SMS'. CJR thanks Alastair Edge for useful discussions around the high-frequency data available in the literature. We also thank our anonymous referee for their careful and constructive feedback which has strengthened this work.

The MeerKAT telescope is operated by the South African Radio Astronomy Observatory, which is a facility of the National Research Foundation, an agency of the Department of Science and Innovation. CJR wishes to acknowledge the assistance of the MeerKAT science operations team in both preparing for and executing the observations that made this work (and the remainder of project MKT-20126) possible.

LOFAR is the Low Frequency Array designed and constructed by ASTRON. It has observing, data processing, and data storage facilities in several countries, which are owned by various parties (each with their own funding sources), and which are collectively operated by the ILT foundation under a joint scientific policy. The ILT resources have benefited from the following recent major funding sources: CNRS-INSU, Observatoire de Paris and Université d'Orléans, France; BMBF, MIWF-NRW, MPG, Germany; Science Foundation Ireland (SFI), Department of Business, Enterprise and Innovation (DBEI), Ireland; NWO, The Netherlands; The Science and Technology Facilities Council, UK; Ministry of Science and Higher Education, Poland; The Istituto Nazionale di Astrofisica (INAF), Italy.

This research made use of the Dutch national e-infrastructure with support of the SURF Cooperative (e-infra 180169) and the LOFAR e-infra group. The Jülich LOFAR Long-Term Archive and the German LOFAR network are both coordinated and operated by the Jülich Supercomputing Centre (JSC), and computing resources on the supercomputer JUWELS at JSC were provided by the Gauss Centre for Supercomputing e.V. (grant CHTB00) through the John von Neumann Institute for Computing (NIC).

This research made use of the University of Hertfordshire high-performance computing facility and the LOFAR-UK computing facility located at the University of Hertfordshire and supported by STFC [ST/P000096/1], and of the Italian LOFAR IT computing infrastructure supported and operated by INAF, and by the Physics Department of Turin university (under an agreement with Consorzio Interuniversitario per la Fisica Spaziale) at the C3S Supercomputing Centre, Italy.

This research has made use of the VLASS QLimage cutout server at cutouts.cirada.ca, operated by the CIRADA. CIRADA is funded by a grant from the Canada Foundation for Innovation 2017 Innovation Fund (Project 35999), as well as by the Provinces of Ontario, British Columbia, Alberta, Manitoba, and Quebec, in collaboration with the National Research Council of Canada, the US National Radio Astronomy Observatory and Australia's Commonwealth Scientific and Industrial Research Organisation.

Funding for the Sloan Digital Sky Survey IV has been provided by the Alfred P. Sloan Foundation, the U.S. Department of Energy Office of Science, and the Participating Institutions. SDSS-

Downloaded from https://academic.oup.com/mnras/article/512/3/4210/6547010 by guest on 07 March 2025

IV acknowledges support and resources from the Center for High Performance Computing at the University of Utah. The SDSS website is www.sdss.org.

SDSS-IV is managed by the Astrophysical Research Consortium for the Participating Institutions of the SDSS Collaboration, including the Brazilian Participation Group, the Carnegie Institution for Science, Carnegie Mellon University, Center for Astrophysics | Harvard & Smithsonian, the Chilean Participation Group, the French Participation Group, Instituto de Astrofísica de Canarias, The Johns Hopkins University, Kavli Institute for the Physics and Mathematics of the Universe (IPMU) / University of Tokyo, the Korean Participation Group, Lawrence Berkeley National Laboratory, Leibniz Institut für Astrophysik Potsdam (AIP), Max-Planck-Institut für Astronomie (MPIA Heidelberg), Max-Planck-Institut für Astrophysik (MPA Garching), Max-Planck-Institut für Extraterrestrische Physik (MPE), National Astronomical Observatories of China, New Mexico State University, New York University, University of Notre Dame, Observatário Nacional / MCTI, The Ohio State University, Pennsylvania State University, Shanghai Astronomical Observatory, United Kingdom Participation Group, Universidad Nacional Autónoma de México, University of Arizona, University of Colorado Boulder, University of Oxford, University of Portsmouth, University of Utah, University of Virginia, University of Washington, University of Wisconsin, Vanderbilt University, and Yale University.

Finally, we wish to acknowledge the developers of the following PYTHON packages (not mentioned explicitly in the text), which were used extensively during this project: APLPY (Robitaille & Bressert 2012), ASTROPY (Astropy Collaboration 2013), CMASHER (van der Velden 2020), COLORCET (Kovesi 2015), MATPLOTLIB (Hunter 2007), NUMPY (van der Walt, Colbert & Varoquaux 2011), and SCIPY (Jones et al. 2001).

DATA AVAILABILITY

The images underlying this article will be shared on reasonable request to the corresponding author. Raw MeerKAT visibilities from MKT-20126 are currently proprietary, with public release nominally scheduled for December 2022; upon release, they can be accessed via the SARAO archive (https://apps.sarao.ac.za/katpaws/archive-search). Raw LOFAR visibilities can be accessed via the LOFAR Long-Term Archive (LTA; https://lta.lofar.eu). The *Chandra* data are available via the Chandra Data Archive (https://cxc.harvard.edu/cda/).

REFERENCES

Ahumada R. et al., 2020, ApJS, 249, 3
Allen S. W. et al., 1992, MNRAS, 259, 67
Arnaud K. A., 1996, in Jacoby G. H., Barnes J., eds, ASP Conf. Ser. Vol. 101, Astronomical Data Analysis Software and Systems V. Astron. Soc. Pac, San Francisco, p. 17
Ascasibar Y., Markevitch M., 2006, ApJ, 650, 102
Asplund M., Grevesse N., Sauval A. J., Scott P., 2009, ARA&A, 47, 481
Astropy Collaboration, 2013, A&A, 558, A33
Baars J. W. M., Genzel R., Pauliny-Toth I. I. K., Witzel A., 1977, A&A, 61, 99
Bartalucci I., Mazzotta P., Bourdin H., Vikhlinin A., 2014, A&A, 566, A25
Biava N. et al., 2021, MNRAS, 508, 3995
Bonafede A. et al., 2014, MNRAS, 444, L44
Bonafede A. et al., 2017, MNRAS, 470, 3465
Bonafede A. et al., 2021, ApJ, 907, 32
Bonnassieux E., Tasse C., Smirnov O., Zarka P., 2018, A&A, 615, A66
Bonnassieux E., Edge A., Morabito L., Bonafede A., 2020, A&A, 637, A51
Botteon A. et al., 2020a, MNRAS, 499, L11
Botteon A. et al., 2020b, ApJ, 897, 93
Botteon A. et al., 2021, A&A, 649, A37
Botteon A., Gastaldello F., Brunetti G., 2018, MNRAS, 476, 5591
Boxelaar J. M., van Weeren R. J., Botteon A., 2021, Astron. Comput., 35, 100464
Bravi L., Gitti M., Brunetti G., 2016, MNRAS, 455, L41
Briggs D. S., 1995, PhD thesis, The New Mexico Institute of Mining and Technology
Brunetti G. et al., 2008, Nature, 455, 944
Brunetti G., Jones T. W., 2014, Int. J. Mod. Phys. D, 23, 1430007
Brunetti G., Lazarian A., 2011, MNRAS, 410, 127
Brunetti G., Blasi P., Cassano R., Gabici S., 2004, MNRAS, 350, 1174
Brunetti G., Zimmer S., Zandanel F., 2017, MNRAS, 472, 1506
Bruno L. et al., 2021, A&A, 650, A44
Camilo F. et al., 2018, ApJ, 856, 180
Cassano R., Brunetti G., Setti G., Govoni F., Dolag K., 2007, MNRAS, 378, 1565
Cavagnolo K. W., Donahue M., Voit G. M., Sun M., 2009, ApJS, 182, 12
Cavaliere A., Fusco-Femiano R., 1976, A&A, 500, 95
Cavaliere A., Fusco-Femiano R., 1978, A&A, 70, 677
Clarke A. O. et al., 2019, A&A, 627, A176
Coble K. et al., 2007, AJ, 134, 897
de Gasperin F. et al., 2019, A&A, 622, A5
de Gasperin F. et al., 2022, A&A, 659, A146
Douglass E. M., Blanton E. L., Clarke T. E., Randall S. W., Wing J. D., 2011, ApJ, 743, 199
Douglass E. M., Blanton E. L., Randall S. W., Clarke T. E., Edwards L. O. V., Sabry Z., ZuHone J. A., 2018, ApJ, 868, 121
Duchesne S. W., Johnston-Hollitt M., Wilber A. G., 2021a, Publ. Astron. Soc. Aust., 38, e031
Duchesne S. W., Johnston-Hollitt M., Bartalucci I., 2021b, Publ. Astron. Soc. Aust., 38, e053
Duchesne S. W., Johnston-Hollitt M., Riseley C. J., Bartalucci I., Keel S. R., 2022, MNRAS, 511, 3525
Enßlin T., Pfrommer C., Miniati F., Subramanian K., 2011, A&A, 527, A99
Ettori S., 2000, MNRAS, 318, 1041
Fabian A. C., Sanders J. S., Taylor G. B., Allen S. W., Crawford C. S., Johnstone R. M., Iwasawa K., 2006, MNRAS, 366, 417
Feretti L., Giovannini G., 1996, in Ekers R. D., Fanti C., Padrielli L., eds, Kluwer Academic Publishers, Proc. 175th Symposium of the International Astronomical Union Vol. 175, Extragalactic Radio Sources. p. 333
Ferrari C., Govoni F., Schindler S., Bykov A. M., Rephaeli Y., 2008, Space Sci. Rev., 134, 93
Foreman-Mackey D., Hogg D. W., Lang D., Goodman J., 2013, PASP, 125, 306
Fujita Y., Kohri K., Yamazaki R., Kino M., 2007, ApJ, 663, L61
Ghizzardi S., Rossetti M., Molendi S., 2010, A&A, 516, A32
Ghizzardi S., De Grandi S., Molendi S., 2014, A&A, 570, A117
Giacintucci S., Markevitch M., Venturi T., Clarke T. E., Cassano R., Mazzotta P., 2014, ApJ, 781, 9
Giacintucci S., Markevitch M., Cassano R., Venturi T., Clarke T. E., Brunetti G., 2017, ApJ, 841, 71
Giacintucci S., Markevitch M., Cassano R., Venturi T., Clarke T. E., Kale R., Cuciti V., 2019, ApJ, 880, 70
Gitti M., Brunetti G., Setti G., 2002, A&A, 386, 456
Goodman J., Weare J., 2010, Comm. Appl. Math. Comput. Sci., 5, 65
Govoni F. et al., 2019, Science, 364, 981
Govoni F., Feretti L., 2004, Int. J. Mod. Phys. D, 13, 1549
Govoni F., Enßlin T. A., Feretti L., Giovannini G., 2001, A&A, 369, 441
Govoni F., Murgia M., Markevitch M., Feretti L., Giovannini G., Taylor G. B., Carretti E., 2009, A&A, 499, 371
Hardcastle M. J. et al., 2016, MNRAS, 462, 1910
Hoang D. N. et al., 2019, A&A, 622, A20
Hoang D. N. et al., 2021, A&A, 656, A154
Hodgson T., Bartalucci I., Johnston-Hollitt M., McKinley B., Vazza F., Wittor D., 2021, ApJ, 909, 198
Hogan M. T. et al., 2015, MNRAS, 453, 1201

Downloaded from https://academic.oup.com/mnras/article/512/3/4210/6547010 by guest on 07 March 2025

Hunter J. D., 2007, Comput. Sci. Eng., 9, 90
Ignesti A. et al., 2022, A&A, 659, A20
Ignesti A., 2022, New Astron., 92, 101732
Ignesti A., Brunetti G., Gitti M., Giacintucci S., 2020, A&A, 640, A37
Intema H. T., van der Tol S., Cotton W. D., Cohen A. S., van Bemmel I. M., Röttgering H. J. A., 2009, A&A, 501, 1185
Intema H. T., Jagannathan P., Mooley K. P., Frail D. A., 2017, A&A, 598, A78
Jackson N. et al., 2016, A&A, 595, A86
Jackson N. et al., 2022, A&A, 658, A2
Jaffe W. J., 1977, ApJ, 212, 1
Jonas J., MeerKAT Team, 2016, in MeerKAT Science: On the Pathway to the SKA. Proceedings of Science, p. 10
Jones E., et al., 2001, SciPy: Open source scientific tools for Python, Available at: http://www.scipy.org/
Józsa G. I. G. et al., 2020, Astrophysics Source Code Library, record ascl:2006.014
Józsa G. I. G. et al., 2021, MNRAS, 501, 2704
Kellermann K. I., 1966, Aust. J. Phys., 19, 195
Kelly B. C., 2007, ApJ, 665, 1489
Knowles K. et al., 2022, A&A, 657, A56
Kovesi P., 2015, preprint (arXiv:1509.03700)
Lacy M. et al., 2020, PASP, 132, 035001
Makhathini S., 2018, PhD thesis, Rhodes Univ.
Mao M. Y., Johnston-Hollitt M., Stevens J. B., Wotherspoon S. J., 2009, MNRAS, 392, 1070
Mauch T. et al., 2020, ApJ, 888, 61
Mazzotta P., Giacintucci S., 2008, ApJ, 675, L9
Mazzotta P., Markevitch M., Forman W. R., Jones C., Vikhlinin A., VanSpeybroeck L., 2001a, preprint (pp astro–ph/0108476)
Mazzotta P., Markevitch M., Vikhlinin A., Forman W. R., David L. P., van Speybroeck L., 2001b, ApJ, 555, 205
Mohan N., Rafferty D., 2015, Astrophysics Source Code Library, record ascl:1502.007
Morabito L. K. et al., 2022, A&A, 658, A1
Murgia M., Govoni F., Markevitch M., Feretti L., Giovannini G., Taylor G. B., Carretti E., 2009, A&A, 499, 679
Norris R. P. et al., 2011, Publ. Astron. Soc. Aust., 28, 215
Norris R. P. et al., 2021, Publ. Astron. Soc. Aust., 38, e046
Offringa A. R. et al., 2014, MNRAS, 444, 606
Offringa A. R., Smirnov O., 2017, MNRAS, 471, 301
Osinga E. et al., 2021, A&A, 648, A11
Owen F. N., Rudnick L., Eilek J., Rau U., Bhatnagar S., Kogan L., 2014, ApJ, 794, 24
Pacholczyk A. G., 1970, Radio Astrophysics: Nonthermal Processes in Galactic and Extragalactic Sources. Freeman, San Francisco
Perrott Y. C. et al., 2021, MNRAS, 508, 2862
Pfrommer C., Enßlin T. A., 2004, A&A, 413, 17
Pratley L., Johnston-Hollitt M., Dehghan S., Sun M., 2013, MNRAS, 432, 243
Pratt G. W., Croston J. H., Arnaud M., Böhringer H., 2009, A&A, 498, 361
Raja R. et al., 2020, MNRAS, 493, L28
Rajpurohit K. et al., 2021a, A&A, 646, A135
Rajpurohit K. et al., 2021b, A&A, 654, A41
Reynolds J. E., 1994, ATNF Internal Memo AT/39.3/040, A Revised Flux Scale for the AT Compact Array. Epping NSW, Australia Telescope National Facility
Richard-Laferrière A. et al., 2020, MNRAS, 499, 2934
Robitaille T., Bressert E., 2012, Astrophysics Source Code Library, record ascl:1208.017
Roger R. S., Costain C. H., Bridle A. H., 1973, AJ, 78, 1030
Rossetti M., Eckert D., De Grandi S., Gastaldello F., Ghizzardi S., Roediger E., Molendi S., 2013, A&A, 556, A44
Rossetti M., Gastaldello F., Eckert D., Della Torre M., Pantiri G., Cazzoletti P., Molendi S., 2017, MNRAS, 468, 1917
Sanders J. S. et al., 2016a, MNRAS, 457, 82
Sanders J. S. et al., 2021, preprint (arXiv:2106.14534)
Sanders J. S., 2006, MNRAS, 371, 829
Sanders J. S., Fabian A. C., Russell H. R., Walker S. A., Blundell K. M., 2016b, MNRAS, 460, 1898
Savini F. et al., 2018, MNRAS, 478, 2234
Savini F. et al., 2019, A&A, 622, A24
Scaife A. M. M., Heald G. H., 2012, MNRAS, 423, L30
Shimwell T. W. et al., 2017, A&A, 598, A104
Shimwell T. W. et al., 2019, A&A, 622, A1
Shimwell T. W. et al., 2022, A&A, 659, A1
Smirnov O. M., Tasse C., 2015, MNRAS, 449, 2668
Swarup G., 1990, Indian J. Radio Space Phys., 19, 493
Tasse C. et al., 2018, A&A, 611, A87
Tasse C. et al., 2021, A&A, 648, A1
Tasse C., 2014, A&A, 566, A127
Timmerman R., van Weeren R. J., McDonald M., Ignesti A., McNamara B. R., Hlavacek-Larrondo J., Röttgering H. J. A., 2021, A&A, 646, A38
van Diepen G., Dijkema T. J., Offringa A., 2018, Astrophysics Source Code Library, record ascl:1804.003
van Haarlem M. P. et al., 2013, A&A, 556, A2
van Weeren R. J. et al., 2016, ApJS, 223, 2
van Weeren R. J. et al., 2017, Nature Astron., 1,44
van Weeren R. J. et al., 2021, A&A, 651, A115
van Weeren R. J., de Gasperin F., Akamatsu H., Brüggen M., Feretti L., Kang H., Stroe A., Zandanel F., 2019, Space Sci. Rev., 215, 16
van der Velden E., 2020, J. Open Source Softw., 5, 2004
van der Walt S., Colbert S. C., Varoquaux G., 2011, Comput. Sci. Eng., 13, 22
Venturi T. et al., 2017, A&A, 603, A125
Venturi T., Giacintucci S., Dallacasa D., Cassano R., Brunetti G., Bardelli S., Setti G., 2008, A&A, 484, 327
Vikhlinin A. et al., 2009, ApJ, 692, 1033
Werner N. et al., 2016, MNRAS, 460, 2752
Wilber A. et al., 2018, MNRAS, 473, 3536
Williams W. L. et al., 2016, MNRAS, 460, 2385
Willingale R., Starling R. L. C., Beardmore A. P., Tanvir N. R., O'Brien P. T., 2013, MNRAS, 431, 394
Zandanel F., Pfrommer C., Prada F., 2014, MNRAS, 438, 124
Zarka P. et al., 2020, in Union Radio Scientifique Internationale - General Assembly and Scientific Symposium Avaiable at:https://www.ursi.org/proceedings/procGA20/papers/URSIGASS2020SummaryPaperNenuFARnew.pdf
ZuHone J. A., Markevitch M., Brunetti G., Giacintucci S., 2013, ApJ, 762, 78
ZuHone J. A., Brunetti G., Giacintucci S., Markevitch M., 2015, ApJ, 801, 146

SUPPORTING INFORMATION

Supplementary data are available at *MNRAS* online.

Appendix A. Value-added data for subtracted sources

Please note: Oxford University Press is not responsible for the content or functionality of any supporting materials supplied by the authors. Any queries (other than missing material) should be directed to the corresponding author for the article.

This paper has been typeset from a TEX/LATEX file prepared by the author.

Downloaded from https://academic.oup.com/mnras/article/512/3/4210/6547010 by guest on 07 March 2025